ANALYSIS AND DESIGN OF MULTIPOLE, SUPERCONDUCTING ROTATING ELECTRIC MACHINES FOR SHIP PROPULSION

by

Joseph Vito Minervini

B.S., United States Merchant Marine Academy

(June, 1970)

Submitted in Partial Fulfillment

of the Requirements for the Degree of

Master of Science in Mechanical Engineering

at the

MASSACHUSETTS INSTITUTE OF TECHNOLOGY

February, 1974

Signature of Author: _____

Department of Mechanical Engineering
January 23, 1974

Certified by: _____

Thesis Supervisor

Accepted by: _____

Chairman, Departmental Committee
on Graduate Students

Archives

MASS. INST. TECH.
APR 1 1974
LIBRARIES

ANALYSIS AND DESIGN OF MULTIPOLE, SUPERCONDUCTING ROTATING ELECTRIC MACHINES FOR SHIP PROPULSION

by

Joseph Vito Minervini

Submitted to the Department fo Mechanical Engineering on January 23, 1974, in partial fulfillment of the requirements for the degree of Master of Science in Mechanical Engineering.

ABSTRACT

The use of superconducting electric machines for ship propulsion offers several advantages in increased power density, flexibility of plant layout, and elimination of large reduction gears and propeller shafts.

In this study large diameter, multipole synchronous machines are modeled as linear machines with flat armature and field windings. Full field, inductance, and power rating expressions are developed for a linear geometry and compared with corresponding cylindrical expressions.

A 29.82 M.W., 60 pole, 120 R.P.M. motor is designed from this model and compared with a conventional synchronous motor designed for a ship propulsion system. An analysis of motor starting and synchronizing is also included.

Thesis Supervisor: Philip Thullen

Title: Assistant Professor of Mechanical Engineering

ACKNOWLEDGMENT

I would like to acknowledge the guidance of my advisor, Professor Philip Thullen, who molded my erratic efforts into a somewhat distinct path. Particular thanks go to Doctor Thomas Keim who led me through some rather sticky places, in spite of myself.

TABLE OF CONTENTS

LIST OF FIGURES

LIST OF TABLES

TABLE I

Glossary of Terms

Symbols

A	Cross-sectional area of one pole winding
b	Pole face dimension
$\overline{B}$	Magnetic flux density
$\overline{B}_{sat}$	Shield material saturation flux density
D	Outside diameter of rotor
E_f	RMS open circuit voltage
$\overline{E}$	Electric field intensity
$\overline{F}$	Magnetic force density
g	Air gap dimension
$\overline{H}$	Magnetic field intensity
I_a	Rated RMS armature current
I_f	Rated field current
J_a	Rated armature current density
J_f	Rated field current density
k	Wave number, Chapter IV
K	Sheet current density
ℓ	Pole pitch
L	Straight section length
L_a	Armature phase-a self-inductance
L_d	Damper shield self-inductance
L_f	Field winding self-inductance
L_{ab}	Mutual inductance, phase-a to phase-b
L_{ad}	Mutual inductance, phase-a to damper
M_a	Mutual inductance field to phase a
M	Vertical distance from origin to upper iron shield
N	Vertical distance from origin to lower iron shield
N_{at}	Number of armature winding turns
N_{ft}	Number of field winding turns
n	Positive integers (1,2,3,...) indicating harmonics
p	Number of pole pairs
p	Power rating

TABLE I
(cont'd)

r	Radius
R	Winding or shield radii, subscripted
R_m	Mean radius of field winding
R_t	Damper shield radius
s	Slip
S	Slip factor used in damper shield analysis
S_{wf}	Field winding dimension
S_{wa}	Armature phase winding dimension
t_a	Armature winding thickness
t_f	Field winding thickness
t_d	Damper shield thickness
t_s	Magnetic shield thickness
u	Horizontal coordinate in fixed frame, Figure
V_{tip}	Tip velocity of rotor
V_t	Rated terminal voltage
x_a	Synchronous reactance, per unit with E_f as base voltage
X_a	Synchronous reactance, ohms
X	R_{ai}/R_{ao}
Y	R_{fi}/R_{fo}
α	Distance from x axis to outside of field winding
α	Distance between damper current sheet and armature current sheet
β	Distance from x axis to inside of armature winding
β	Distance between damper current and iron shield
β	$\frac{2A}{R_{fo}}$ (Appendix C)
γ	Distance from x axis to inside of iron shield
δ	Skin depth
δ	Rotor axis displacement from phase a axis, (Figure) cartesian coordinates

TABLE I
(cont'd)

θ	Angular displacement
θ_{wf}	Field winding included angle
θ_{wfe}	$p\theta_{wf}$
θ_{wa}	Armature winding included angle
θ_{wae}	$p\theta_{wa}$
λ	Subscripted, flux linkage
λ	$\frac{n\pi}{\ell}$, Appendix A
μ	Magnetic permeability
σ	Conductivity (mhos/meter)
σ_s	Surface conductivity (mhos)
ϕ	Rotor axis displacement from phase-a axis, cylindrical coordinates
Φ	Scalar potential, Appendix A
ψ	Power factor angle
ω	Angular velocity or frequency

Subscripts

a	Armature winding
a	Phase a
b	Phase b
c	Phase c
d	Damper
f	Field winding
i	Inner, inside
m	Mutual
o	Outer, outside
s	Shield
w	Winding
w	Within

TABLE I

(cont'd)

Superscripts

a	Damper shield analysis, region between iron shield and armature current sheet
b	Damper shield analysis, region between armature current sheet and damper current sheet
c	Damper shield analysis, region below damper current sheet

Chapter I. Introduction

The application of superconductors to rotating electric machinery promises advantages over conventional electric machine technology. This is especially true in the use of superconducting electric generators and motors for marine propulsion systems.

In general, superconducting electric propulsion plants with gas turbine prime movers offer many advantages over steam turbine systems and diesel engines in weight and volume reduction of the overall system. Also, the elimination of large, direct mechanical reduction gears and long propulsion shafts results in a highly desirable flexibility of component placement. Gas turbine-generator set units can be placed in positions readily accessible for easy maintenance, and intake and exhaust ducting lengths may be considerably decreased. Motors can be directly coupled to the propeller shafts. For certain high performance craft, entire steerable pods containing motor and propeller may be practical. In large propulsion systems the parallel operation of several generators and motors offers a wide range of operating modes for different load, speed, and emergency conditions.

The technical and economic reasons for considering superconducting electric propulsion systems are many. However, there are some important problems that must be

overcome. Ship drive systems must be capable of operating at several different maneuvering speeds between zero and normal cruising speed. In electric systems this can be accomplished by several different methods. One of these is by varying the electrical frequency of the motor by means of a frequency or cycloconvertor. Another method is to have the motor-generator speed ratio fixed by the field-pole ratio of the two machines in a synchronous system and then affect propeller speed changes by varying the prime mover speed. This results in inefficient operation of the prime mover during maneuvering operations involving many speed changes. However, for normal commercial vessels, the time spent maneuvering is only a small fraction of the time spent at normal cruising speeds where the system is designed for optimum efficiency.

This work is concerned with solving the problems encountered in the design of a large power rating, slow speed, multipole, synchronous electric motor for use with a synchronous generator. In this type of system a large speed reduction is necessary for the efficient operation of a high speed prime mover, such as a gas turbine, coupled with the relatively slow speed propeller. This requires a large number of field poles on the motor. For large power requirements, the problem, then, is to get enough of the flux created in the field windings to link the armature

windings. Electric machines with large air gap to pole pitch ratios have a large amount of leakage flux if not properly designed. Conventional machines have iron in the rotor core and stator flux circuits to enhance flux linkage with the armature windings and reduce leakage flux. Iron is not used in superconducting machines because the high magnetic fields created would exceed the saturation limit.

Early efforts in this study to solve this problem centered on non-conventional geometries to improve flux linkage, and these may be found in Appendix C. However, this approach did not yield very encouraging results. Therefore, the principal approach taken was to model a large diameter, multipole, cylindrical machine as a flat stationary armature and a flat, moving field winding. This proved to be a good simplified model. The field expressions developed from this model can be reduced to a very simplified form which is easy to use and understand. The effects of changing certain design parameters are readily computed. This yields a relatively easy method for the first rough design of large, multipole synchronous electric machines.

The next step taken was the design of a superconducting motor based on these results and a comparison of this design with a conventional ship propulsion motor proposed by one of the major electric machinery manufacturers. This is primarily an electrical design with minimum consideration given to the mechanical and thermal design.

Chapter II. Linear Analogy of Large, Multipole, Synchronous Machines.

A linear (flat) stationary armature and moving linear field winding were used to model the stationary armature and rotating field winding of a large diameter, multipole, cylindrical synchronous electric machine. Field expressions were derived for a flat, three phase, armature winding and flat field winding with ferromagnetic upper and lower shields. Figure 1 shows the physical configuration. The derivations are presented in Appendix A and the results are summarized in Table II.

This is a two-dimensional analysis. The field expressions were done on a per-unit length basis, and actual end-turn effects were not analyzed.

The actual physical arrangement of a superconducting machine can be modeled mathematically by setting the lower iron shield at an infinite distance from the field winding. This leaves the moving field winding, stationary armature and the upper iron shield as the components of the machine. Except for the upper iron shield, there is no ferromagnetic material in the machine. These expressions may be simplified even further by placing the upper iron shield at infinity. The form of the field expressions demonstrates explicitly the field variations in the x and y directions.

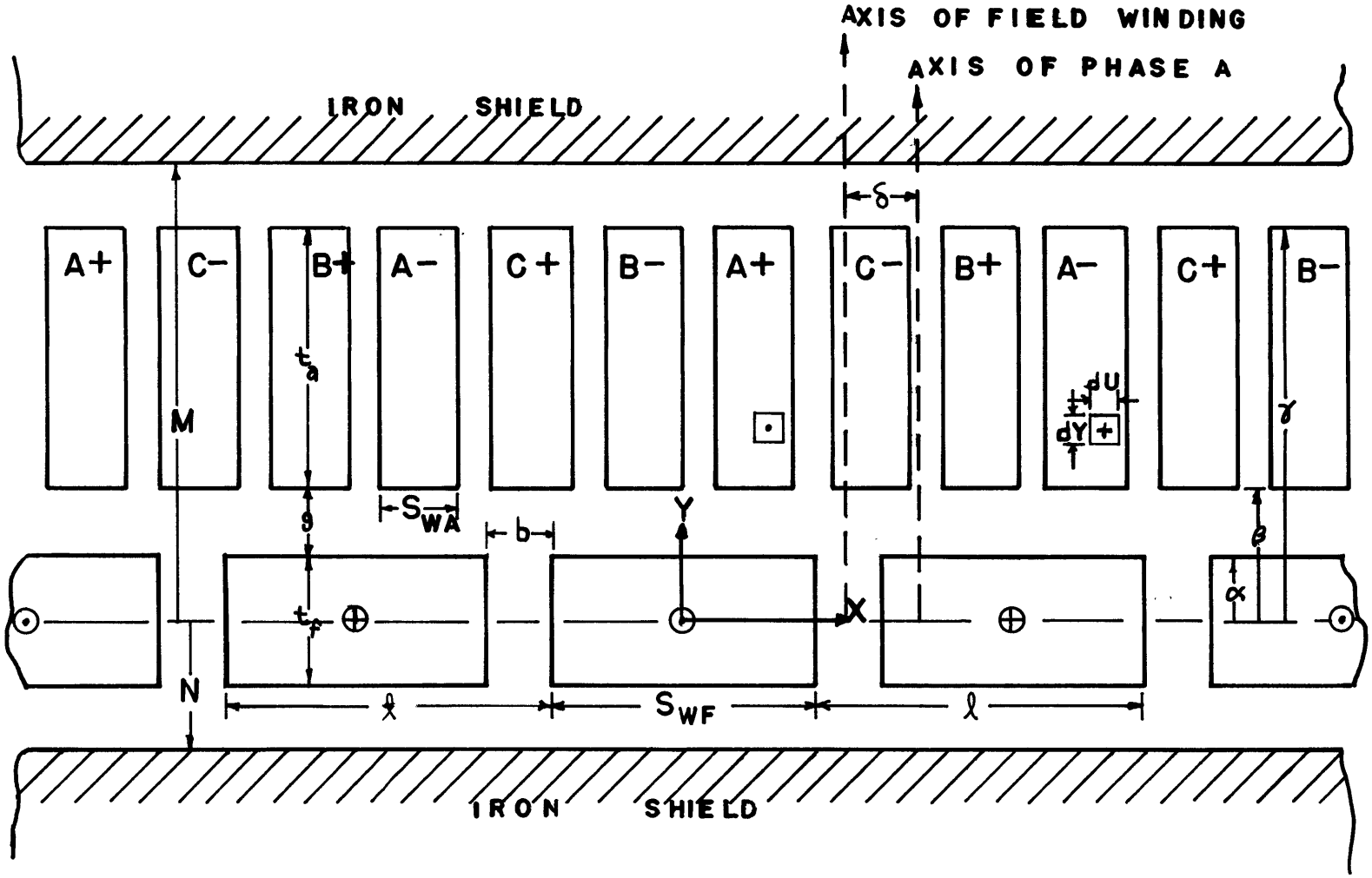

FIG 1 FIELD AND ARMATURE CONFIGURATION

TABLE II

FIELD EXPRESSIONS FOR LINEAR WINDING GEOMETRY

$N \leq y \leq -t_f/2$

$$H_{xfi} = \sum_{n\ odd} \frac{4J_f\ell}{n^2\pi^2} \sin\left(\frac{n\pi S_{wf}}{2\ell}\right) \frac{\left(1+e^{\frac{-2n\pi M}{\ell}}\right)}{\left(e^{\frac{-2n\pi M}{\ell}} - e^{\frac{-2n\pi N}{\ell}}\right)} \sinh\left(\frac{n\pi t_f}{2\ell}\right) \quad X$$

$$\left[e^{\frac{-n\pi y}{\ell}} - e^{\frac{n\pi}{\ell}(y-2N)}\right] \cos\left(\frac{n\pi x}{\ell}\right)$$

$$H_{yfi} = \sum_{n\ odd} \frac{4J_f\ell}{n^2\pi^2} \sin\left(\frac{n\pi S_{wf}}{2\ell}\right) \frac{\left(1+e^{\frac{-2n\pi M}{\ell}}\right)}{\left(e^{\frac{-2n\pi M}{\ell}} - e^{\frac{-2n\pi N}{\ell}}\right)} \sinh\left(\frac{n\pi t_f}{2\ell}\right) \quad X$$

$$\left[e^{\frac{n\pi}{\ell}(y-2N)} + e^{\frac{-n\pi y}{\ell}}\right] \sin\left(\frac{n\pi x}{\ell}\right)$$

$-t_f/2 \leq y \leq +t_f/2$

$$H_{xfw} = \sum_{n\ odd} \frac{4J_f\ell}{n^2\pi^2} \frac{\sin\left(\frac{n\pi S_{wf}}{2\ell}\right)}{\left(e^{\frac{-2n\pi M}{\ell}} - e^{\frac{-2n\pi N}{\ell}}\right)} \left\{\sinh\left(\frac{n\pi t_f}{2\ell}\right)\left[e^{\frac{-n\pi y}{\ell}} - e^{\frac{n\pi}{\ell}(y-2M-2N)}\right] + \right.$$

$$\left. \sinh\left(\frac{n\pi y}{\ell}\right)\left[e^{\frac{-n\pi}{\ell}(t_f/2+2N)} - e^{\frac{n\pi}{\ell}(t_f/2-2M)}\right]\right\} \cos\left(\frac{n\pi x}{\ell}\right)$$

$$H_{yfw} = \sum_{n\ odd} \frac{4J_f\ell}{n^2\pi^2} \frac{\sin\left(\frac{n\pi S_{wf}}{2\ell}\right)}{\left(e^{\frac{-2n\pi M}{\ell}} - e^{\frac{-2n\pi N}{\ell}}\right)} \left\{\left(e^{\frac{-2n\pi M}{\ell}} - e^{\frac{-2n\pi N}{\ell}}\right) + \right.$$

$$\left. \cosh\left(\frac{n\pi y}{\ell}\right)\left[e^{\frac{-n\pi}{\ell}\left(\frac{t_f}{2}+2N\right)} - e^{\frac{n\pi}{\ell}\left(\frac{t_f}{2}-2M\right)}\right] - \sinh\left(\frac{n\pi t_f}{2\ell}\right)\left[e^{\frac{n\pi}{\ell}(y-2M-2N)} + e^{\frac{-n\pi y}{\ell}}\right]\right\} \sin\left(\frac{n\pi x}{\ell}\right)$$

$+t_f/2 \leq y \leq M$

$$H_{xfo} = \sum_{n\,odd} \frac{4J_f \ell}{n^2\pi^2} \sin\left(\frac{n\pi S_{wf}}{2\ell}\right) \frac{\left(1+e^{\frac{-2n\pi N}{\ell}}\right)}{\left[e^{\frac{-2n\pi M}{\ell}} - e^{\frac{-2n\pi N}{\ell}}\right]} \sinh\left(\frac{n\pi t_f}{2\ell}\right) \quad X$$

$$\left[e^{\frac{-n\pi y}{\ell}} - e^{\frac{n\pi}{\ell}(y-2M)}\right] \cos\left(\frac{n\pi x}{\ell}\right)$$

$$H_{yfo} = \sum_{n\,odd} \frac{4J_f \ell}{n^2\pi^2} \sin\left(\frac{n\pi S_{wf}}{2\ell}\right) \frac{\left(1+e^{\frac{-2n\pi N}{\ell}}\right)}{\left[e^{\frac{-2n\pi M}{\ell}} - e^{\frac{-2n\pi N}{\ell}}\right]} \sinh\left(\frac{n\pi t_f}{2\ell}\right) \quad X$$

$$\left[e^{\frac{n\pi}{\ell}(y-2M)} + e^{\frac{-n\pi y}{\ell}}\right] \sin\left(\frac{n\pi x}{\ell}\right)$$

TABLE IIB

FIELD EXPRESSIONS WITHOUT LOWER SHIELD

(lim N → -∞)

$y \leq -t_f/2$

$$H_{xfi} = \sum_{n\,odd} \frac{4J_f \ell}{n^2\pi^2} \sin\left(\frac{n\pi S_{wf}}{2\ell}\right) \sinh\left(\frac{n\pi t_f}{2\ell}\right) \left[\left(1+e^{\frac{-2n\pi M}{\ell}}\right)e^{\frac{n\pi y}{\ell}}\right] \cos\left(\frac{n\pi x}{\ell}\right)$$

$$H_{yfi} = \sum_{n\,odd} \frac{4J_f \ell}{n^2\pi^2} \sin\left(\frac{n\pi S_{wf}}{2\ell}\right) \sinh\left(\frac{n\pi t_f}{2\ell}\right) \left[\left(1+e^{\frac{-2n\pi M}{\ell}}\right)e^{\frac{n\pi y}{\ell}}\right] \sin\left(\frac{n\pi x}{\ell}\right)$$

$-t_f/2 \leq y \leq +t_f/2$

$$H_{xfw} = \sum_{n\,odd} \frac{4J_f \ell}{n^2\pi^2} \sin\left(\frac{n\pi S_{wf}}{2\ell}\right) \left[\sinh\left(\frac{n\pi t_f}{2\ell}\right)e^{\frac{n\pi}{\ell}(y-2M)} - \sinh\left(\frac{n\pi y}{\ell}\right)e^{\frac{-n\pi t_f}{2\ell}}\right] \cos\left(\frac{n\pi x}{\ell}\right)$$

$$H_{yfw} = \sum_{n\,odd} \frac{4J_f \ell}{n^2\pi^2} \sin\left(\frac{n\pi S_{wf}}{2\ell}\right) \left[1+\sinh\left(\frac{n\pi t_f}{2\ell}\right)e^{\frac{n\pi}{\ell}(y-2M)} - \cosh\left(\frac{n\pi y}{\ell}\right)e^{\frac{-n\pi t_f}{2\ell}}\right] \sin\left(\frac{n\pi x}{\ell}\right)$$

$+t_f/2 \leq y \leq M$

$$H_{xfo} = \sum_{n\,odd} \frac{4J_f \ell}{n^2\pi^2} \sin\left(\frac{n\pi S_{wf}}{2\ell}\right) \sinh\left(\frac{n\pi t_f}{2\ell}\right) \left[e^{\frac{n\pi}{\ell}(y-2M)} - e^{\frac{-n\pi y}{\ell}}\right] \cos\left(\frac{n\pi x}{\ell}\right)$$

$$H_{yfo} = \sum_{n\,odd} \frac{4J_f \ell}{n^2\pi^2} \sin\left(\frac{n\pi S_{wf}}{2\ell}\right) \sinh\left(\frac{n\pi t_f}{2\ell}\right) \left[e^{\frac{n\pi}{\ell}(y-2M)} + e^{\frac{-n\pi y}{\ell}}\right] \sin\left(\frac{n\pi x}{\ell}\right)$$

TABLE IIC

FIELD EXPRESSIONS WITH NO IRON SHIELDS

(lim M → ∞)
(lim N → -∞)

$y \leq -t_f/2$

$$H_{xfi} = \sum_{n\,odd} \frac{4J_f \ell}{n^2\pi^2} \sin\left(\frac{n\pi S_{wf}}{2\ell}\right) \sinh\left(\frac{n\pi t_f}{2\ell}\right) e^{\frac{n\pi y}{\ell}} \cos\left(\frac{n\pi x}{\ell}\right)$$

$$H_{yfi} = \sum_{n\,odd} \frac{4J_f \ell}{n^2\pi^2} \sin\left(\frac{n\pi S_{wf}}{2\ell}\right) \sinh\left(\frac{n\pi t_f}{2\ell}\right) e^{\frac{n\pi y}{\ell}} \sin\left(\frac{n\pi x}{\ell}\right)$$

$-t_f/2 \leq y \leq +t_f/2$

$$H_{xfw} = \sum_{n\,odd} \frac{4J_f \ell}{n^2\pi^2} \sin\left(\frac{n\pi S_{wf}}{2\ell}\right) \sinh\left(\frac{n\pi y}{\ell}\right) e^{\frac{-n\pi t_f}{2\ell}} \cos\left(\frac{n\pi x}{\ell}\right)$$

$$H_{yfw} = \sum_{n\,odd} \frac{4J_f \ell}{n^2\pi^2} \sin\left(\frac{n\pi S_{wf}}{2\ell}\right) \left[1 - \cosh\left(\frac{n\pi y}{\ell}\right) e^{\frac{-n\pi t_f}{2\ell}}\right] \sin\left(\frac{n\pi x}{\ell}\right)$$

$y \leq +t_f/2$

$$H_{xfo} = \sum_{n\ \text{odd}} \frac{4J_f \ell}{n^2\pi^2} \sin\left(\frac{n\pi S_{wf}}{2\ell}\right) \sinh\left(\frac{n\pi t_f}{2\ell}\right) e^{\frac{-n\pi y}{\ell}} \cos\left(\frac{n\pi x}{\ell}\right)$$

$$H_{yfo} = \sum_{n\ \text{odd}} \frac{4J_f \ell}{n^2\pi^2} \sin\left(\frac{n\pi S_{wf}}{2\ell}\right) \sinh\left(\frac{n\pi t_f}{2\ell}\right) e^{\frac{-n\pi y}{\ell}} \sin\left(\frac{n\pi x}{\ell}\right)$$

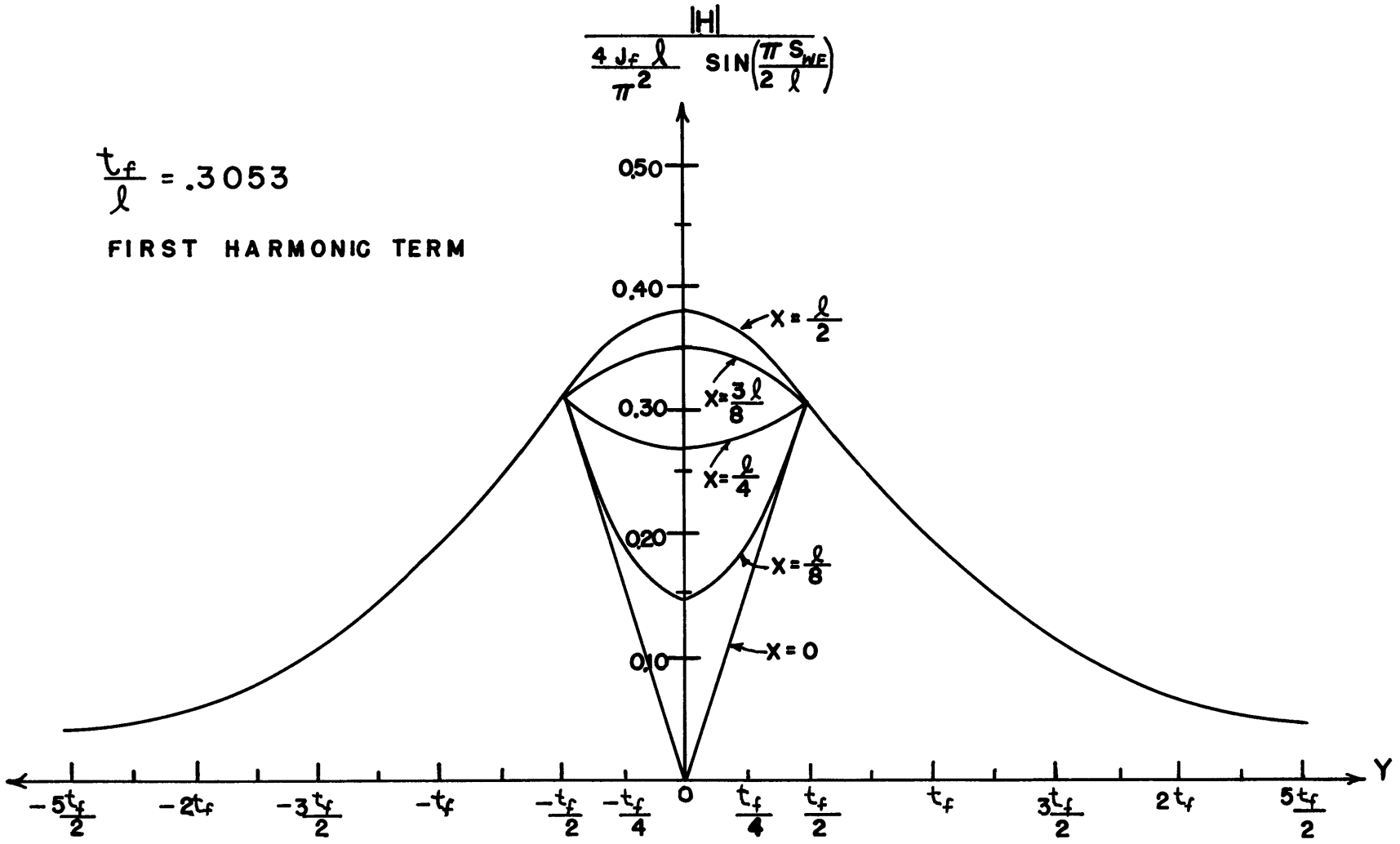

FIG. 2 FIELD INTENSITY VARIATION IN Y-DIRECTION

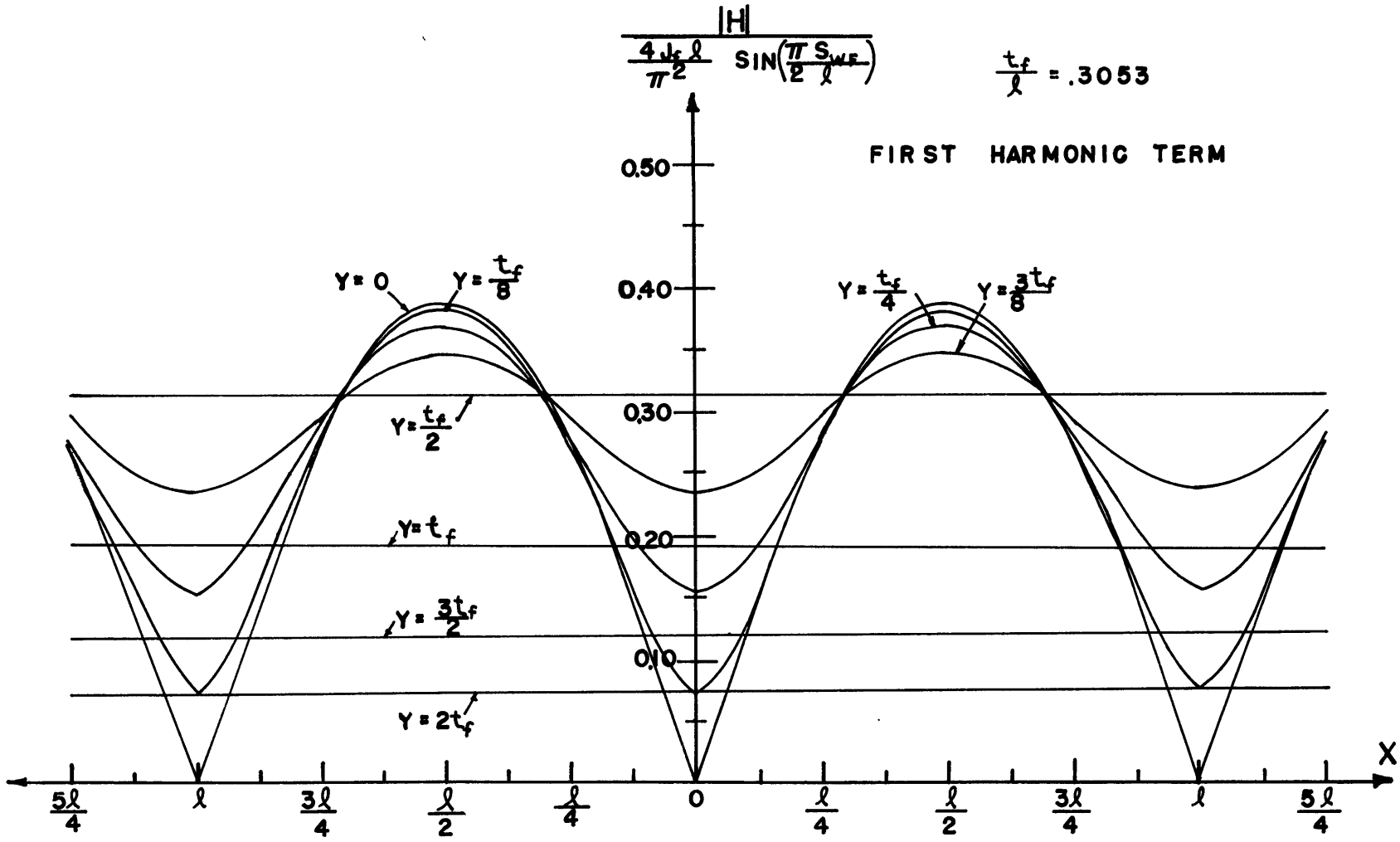

FIG. 3 FIELD INTENSITY VARIATION IN X-DIRECTION

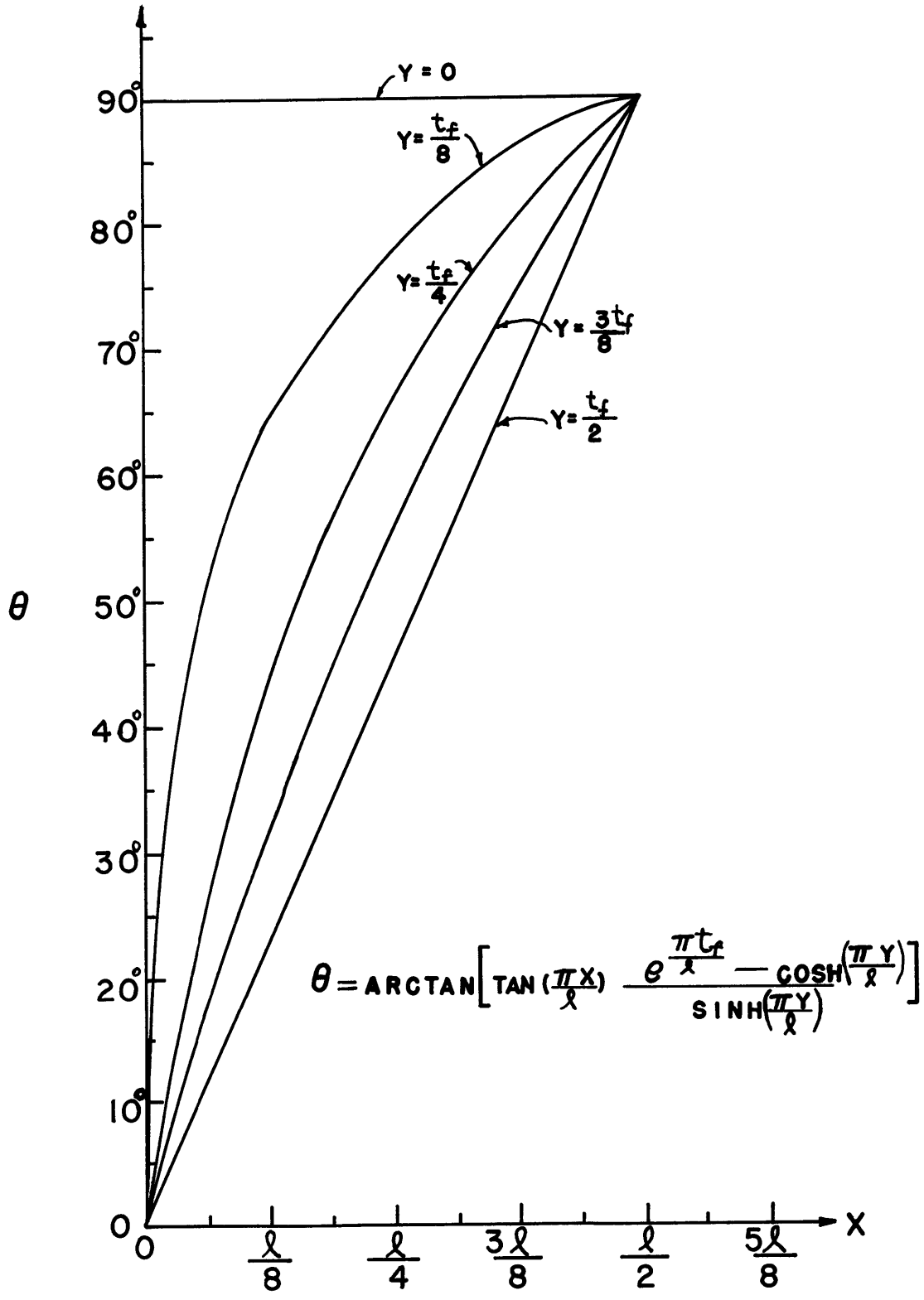

FIG. 4 ANGULAR ORIENTATION OF FIELD

TABLE III

SELF AND MUTUAL INDUCTANCE EXPRESSIONS FOR LINEAR WINDING GEOMETRY

$$N' = N + \left(g + \frac{t_f}{2} + \frac{t_a}{2}\right) \qquad M' = M - \left(g + \frac{t_f}{2} + \frac{t_a}{2}\right)$$

$$\frac{M_{af}}{pL} = -\sum_{n\,\text{odd}} \frac{16\mu_o \ell^4}{n^5\pi^5} \left(\frac{N_{ft}}{S_{wf}t_f}\right) \sin\left(\frac{n\pi S_{wf}}{2\ell}\right) \left(\frac{N_{at}}{S_{wa}t_a}\right) \sin\left(\frac{n\pi S_{wa}}{2\ell}\right) \cos\left(\frac{n\pi\delta}{\ell}\right) \quad X$$

$$\frac{\left(1+e^{\frac{-2n\pi N}{\ell}}\right)}{\left(e^{\frac{-2n\pi M}{\ell}} - e^{\frac{-2n\pi N}{\ell}}\right)} \sinh\left(\frac{n\pi t_f}{2\ell}\right) \left[e^{\frac{-2n\pi M}{\ell}}\left(e^{\frac{n\pi\gamma}{\ell}} - e^{\frac{n\pi\beta}{\ell}}\right) + \left(e^{\frac{-n\pi\beta}{\ell}} - e^{\frac{-n\pi\gamma}{\ell}}\right)\right]$$

$$\frac{L_f}{pL} = \sum_{n\,\text{odd}} \frac{32\mu_o \ell^4}{n^5\pi^5} \left(\frac{N_{ft}}{S_{wf}t_f}\right)^2 \sin^2\left(\frac{n\pi S_{wf}}{2\ell}\right) \left\{\frac{n\pi t_f}{2\ell} + \sin\left(\frac{n\pi t_f}{2\ell}\right) \frac{\left[e^{\frac{-n\pi}{\ell}\left(\frac{t_f}{2}+2N\right)} - e^{\frac{n\pi}{\ell}\left(\frac{t_f}{2}-2M\right)}\right]}{\left(e^{\frac{-2n\pi M}{\ell}} - e^{\frac{-2n\pi N}{\ell}}\right)}\right.$$

$$\left. - \sinh^2\left(\frac{n\pi t_f}{2\ell}\right) \frac{\left[1+e^{\frac{-n\pi}{\ell}(2M+2N)}\right]}{\left(e^{\frac{-2n\pi M}{\ell}} - e^{\frac{-2n\pi N}{\ell}}\right)}\right\}$$

$$\frac{L_a}{pL} = \sum_{n\,\text{odd}} \frac{32\mu_o \ell^4}{n^5\pi^5} \left(\frac{N_{at}}{S_{wa}t_a}\right)^2 \sin^2\left(\frac{n\pi S_{wa}}{2\ell}\right) \left\{\frac{n\pi t_a}{2\ell} + \sinh\left(\frac{n\pi t_a}{2\ell}\right) \frac{\left[e^{\frac{-n\pi}{\ell}\left(\frac{t_a}{2}+2N'\right)} - e^{\frac{n\pi}{\ell}\left(\frac{t_a}{2}-2M'\right)}\right]}{\left(e^{\frac{-2n\pi M'}{\ell}} - e^{\frac{-2n\pi N'}{\ell}}\right)}\right.$$

$$\left. - \sinh^2\left(\frac{n\pi t_a}{2\ell}\right) \frac{\left[1+e^{\frac{-n\pi}{\ell}(2M'+2N')}\right]}{\left(e^{\frac{-2n\pi M'}{\ell}} - e^{\frac{-2n\pi N'}{\ell}}\right)}\right\}$$

$$\frac{L_{ab}}{pL} = \sum_{n\,\text{odd}} \frac{32\mu_o \ell^4}{n^5\pi^5} \left(\frac{N_{ta}}{S_{wa}t_a}\right)^2 \sin^2\left(\frac{n\pi S_{wa}}{2\ell}\right) \cos\left(\frac{2n\pi}{3}\right) \left\{\left(\frac{n\pi t_a}{2\ell}\right) + \right.$$

$$\left. \sinh\left(\frac{n\pi t_a}{2\ell}\right) \frac{\left[e^{\frac{-n\pi}{\ell}\left(\frac{t_a}{2}+2N'\right)} - e^{\frac{n\pi}{\ell}\left(\frac{t_a}{2}-2M'\right)}\right]}{\left(e^{\frac{-2n\pi M'}{\ell}} - e^{\frac{-2n\pi N'}{\ell}}\right)} - \sinh^2\left(\frac{n\pi t_a}{2\ell}\right) \frac{\left(1+e^{\frac{-n\pi}{\ell}(2M'+2N')}\right)}{\left(e^{\frac{-2n\pi M'}{\ell}} - e^{\frac{-2n\pi N'}{\ell}}\right)}\right\}$$

(All inductances are for one pole pair)

Figures 2 and 3 show graphically how field intensity, $\bar{H}$, varies in these directions. The variation of the field intensity in the y direction is shown in Figure 2. Figure 3 demonstrates the field variation in the x direction. The angular orientation of the field is displayed in Figure 4.

Expressions for the self and mutual inductances of the field and armature windings are derived by integrating the fields over the area of the windings. This is done in Appendix A and presented in Table III. These expressions are also based on a per-unit straight section length.

The field intensity expressions contain terms for armature current density and field current density. These are given by:

$$J_f = \frac{N_{ft}\, I_f}{S_{wf}\, t_f} \qquad \text{and} \qquad J_a = \frac{N_{at}\, I_a}{S_{wa}\, t_a}$$

where I_a is the r.m.s. value of armature terminal current.

Power Rating

With these expressions we can now derive a power rating for the linear geometry machine.

$$P = 3V_t I_t = 3E_f I_t \left(\frac{V_t}{E_f}\right)$$

V_t is rated terminal voltage, I_t is related to current density by the armature winding geometry and E_f is generated internal voltage, given by:

$$E_f = \frac{\omega_e M_1 I_f}{\sqrt{2}} \qquad \omega_e = \frac{\pi V_{tip}}{\ell}$$

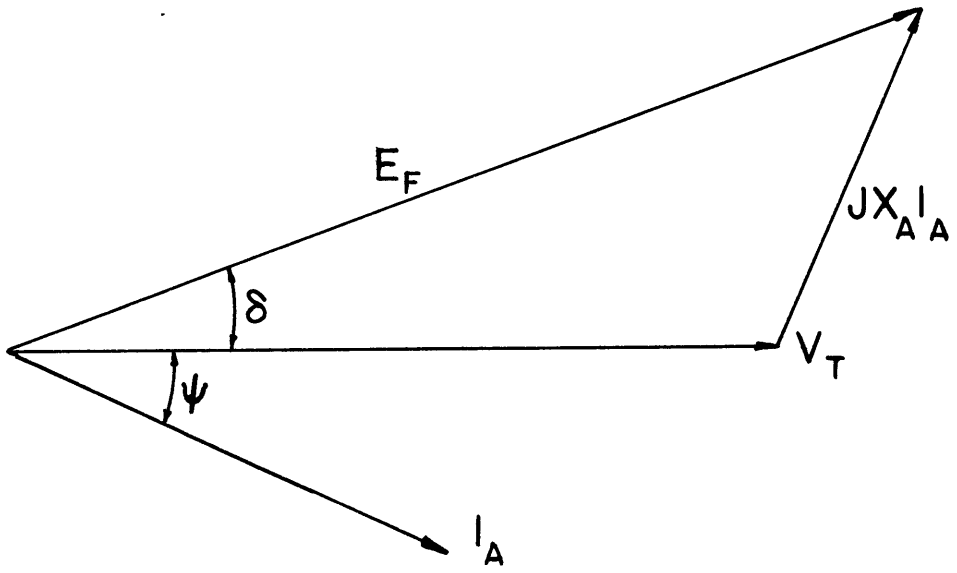

FIG. 5 VOLTAGE CURRENT RELATIONSHIP

E_f is the r.m.s. value and V_{tip} is the velocity of the moving field winding. Power then is:

$$P = \frac{48}{\sqrt{2}} \omega_e \mu_o J_f J_a L \frac{\ell^4}{\pi^5} \sin\left(\frac{\pi S_{wf}}{2\ell}\right)\sin\left(\frac{\pi S_{wa}}{2\ell}\right) \frac{\left[1+\exp\left(\frac{-2\pi M}{\ell}\right)\right]}{\left(e^{\frac{-2\pi M}{\ell}} - e^{\frac{-2\pi N}{\ell}}\right)}$$

$$X \sinh\left(\frac{\pi t_f}{2\ell}\right) \left[e^{\frac{-2\pi M}{\ell}} \left(e^{\frac{\pi\beta}{\ell}} - e^{\frac{\pi\gamma}{\ell}}\right) + \left(e^{\frac{-\pi\gamma}{\ell}} - e^{\frac{-\pi\beta}{\ell}}\right)\right] \left(\frac{V_t}{E_f}\right)$$

where $\gamma = g + \frac{t_f}{2} + t_a$ and $\beta = g + \frac{t_f}{2}$

As there is no iron within the field winding of a superconducting machine, we can simplify this by removing the lower iron shield.

$\lim N \longrightarrow -\infty$

$$P = \frac{48}{\sqrt{2}} \frac{\ell^4}{\pi^5} \omega_e \mu_o J_f J_a L \sin\left(\frac{\pi S_{wf}}{2\ell}\right) \sin\left(\frac{\pi S_{wa}}{2\ell}\right) \sinh\left(\frac{\pi t_f}{2\ell}\right) X$$

$$\left[e^{\frac{-2\pi M}{\ell}} \left(e^{\frac{\pi\gamma}{\ell}} - e^{\frac{\pi\beta}{\ell}}\right) + \left(e^{\frac{-\pi\beta}{\ell}} - e^{\frac{-\pi\gamma}{\ell}}\right)\right] \left(\frac{V_t}{E_f}\right)$$

and $\left(\frac{V_t}{E_f}\right) = \sqrt{1 - X_a^2 \cos\psi} - X_a \sin\psi$

(See Figure 5)

Cos ψ is the power factor and x_a is per-unit synchronous reactance with E_f as base voltage.

$$x_a = \frac{X_a I_a}{E_f}$$

$$x_a = \frac{\omega_e (L_a - L_{ab}) I_a}{E_f} = \frac{\sqrt{2}\,(L_a - L_{ab}) I_a}{M \quad I_f}$$

Figure 5 shows the voltage-current relationship.

For first harmonic terms only, and no iron shields ($\lim N \longrightarrow -\infty$, $M \longrightarrow +\infty$), this expression becomes:

$$X_a = 3\sqrt{2}\,\frac{L_a}{L_m}\,\frac{J_a}{J_f}\,\frac{\sin\left(\frac{\pi S_{wa}}{2\ell}\right)}{\sin\left(\frac{\pi S_{wf}}{2\ell}\right)}\,\frac{\frac{\pi t_a}{\ell} - \left(1 - e^{-\frac{\pi t_a}{\ell}}\right)}{\left(1-e^{-\frac{\pi t_a}{\ell}}\right)\left(1-e^{-\frac{\pi t_f}{\ell}}\right)}\,(e^{\pi g/\ell})$$

This expression, along with the simplified power rating expression ($\lim \begin{matrix} M \longrightarrow \infty \\ N \longrightarrow -\infty \end{matrix}$)

$$P = \frac{24\,\ell^4}{\sqrt{2}\,\pi^5}\,\omega\,\mu_o L_m J_f J_a \sin\left(\frac{\pi S_{wf}}{2\ell}\right) \sin\left(\frac{\pi S_{wa}}{2\ell}\right) \left(1-e^{-\frac{\pi t_f}{\ell}}\right)\left(1-e^{-\frac{\pi t_a}{\ell}}\right)$$

$$X\,\left(e^{-\frac{\pi g}{\ell}}\right)\,\left(\frac{V_t}{E_f}\right)$$

First we can see that the power falls off exponentially with the characteristic air gap dimension, $\frac{\pi g}{\ell}$. It becomes obvious that we should design a machine with the minimum air gap necessary for mechanical clearance.

The term that contains the armature geometry effects, $\left(1-e^{-\frac{\pi t_a}{\ell}}\right)$, indicates that there is a point of diminishing effectiveness for increases of armature thickness, as shown in Figure 6. P_∞ is the power output from a machine with an armature of infinite thickness. An armature thickness can be chosen for the initial design that gives, perhaps, a 90% or 95% effectiveness.

Although the power rating expression has a similar term for the field winding thickness, $\left(1-e^{-\frac{\pi t_f}{\ell}}\right)$, the same criterion of effectiveness cannot be used to determine an optimum field

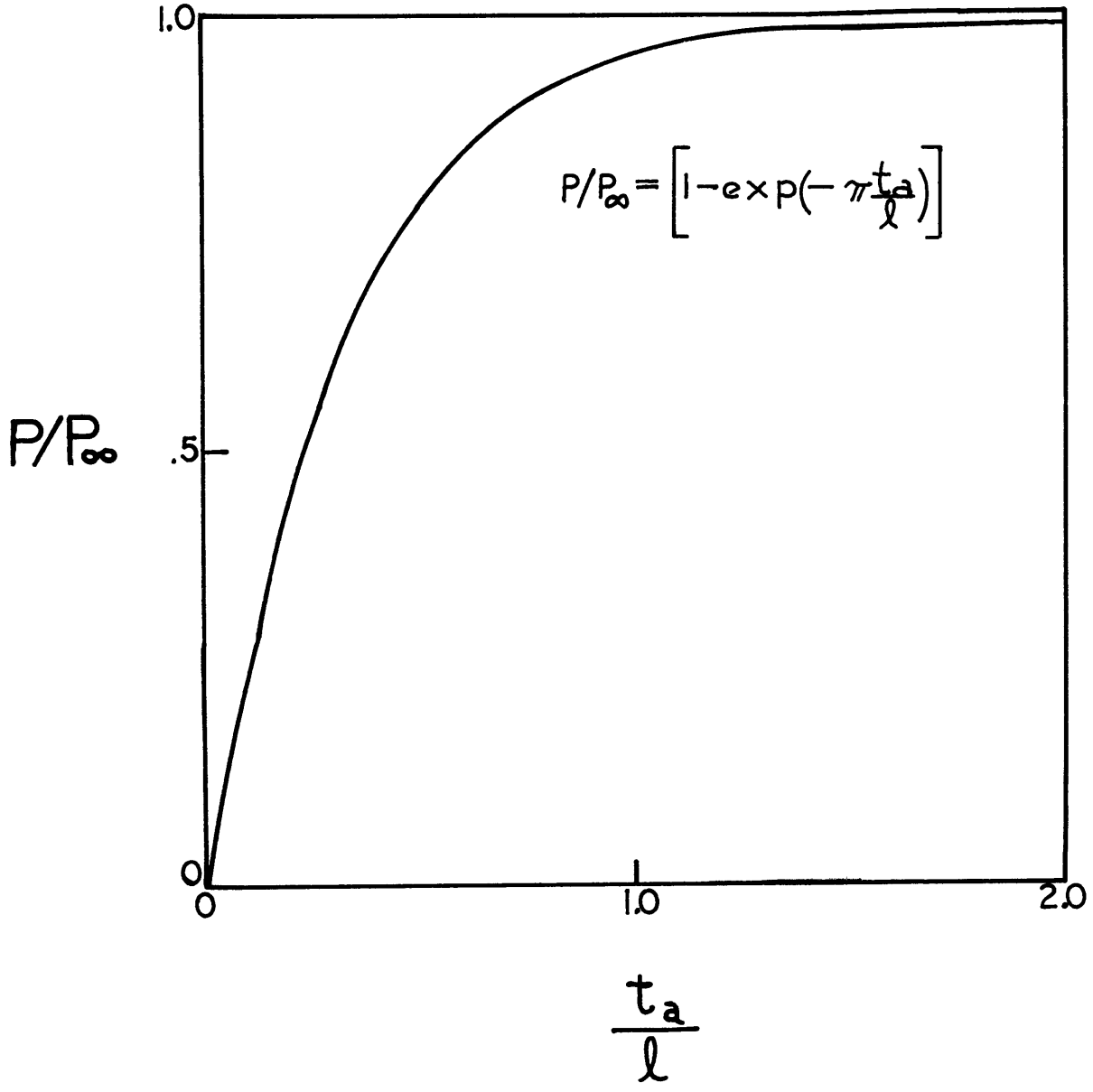

FIG. 6 ARMATURE THICKNESS EFFECTIVENESS

winding dimension. This dimension must be determined by taking into account the maximum field density which occurs within the winding volume.

A superconductor may be driven into the normal region by an excessively strong magnetic field. Therefore, the magnetic characteristics of the superconductor must be known to choose the maximum value of flux density, with sufficient operating margin from the transition line between normal and superconducting regions. The field winding thickness required to achieve this operating point can then be calculated from the field intensity expression for the region within the winding volume.

Power Density

The linear dependence of power rating (or power density) with field current density demonstrates a major advantage of superconducting machines over conventional machines. This is because superconductivity allows the use of much higher field current densities than are possible in conventional machines. Figure 7 demonstrates this point. Power density is the power per active volume of one pole pair.

$$\frac{P}{L_m 2\ell (t_f+g+t_a)} = \text{Power Density}$$

For this particular study certain parameters were fixed. The winding dimension, $\frac{n\pi S_{wf}}{2\ell}$, was chosen so as to make third harmonic fields zero. From Figure 6 the armature

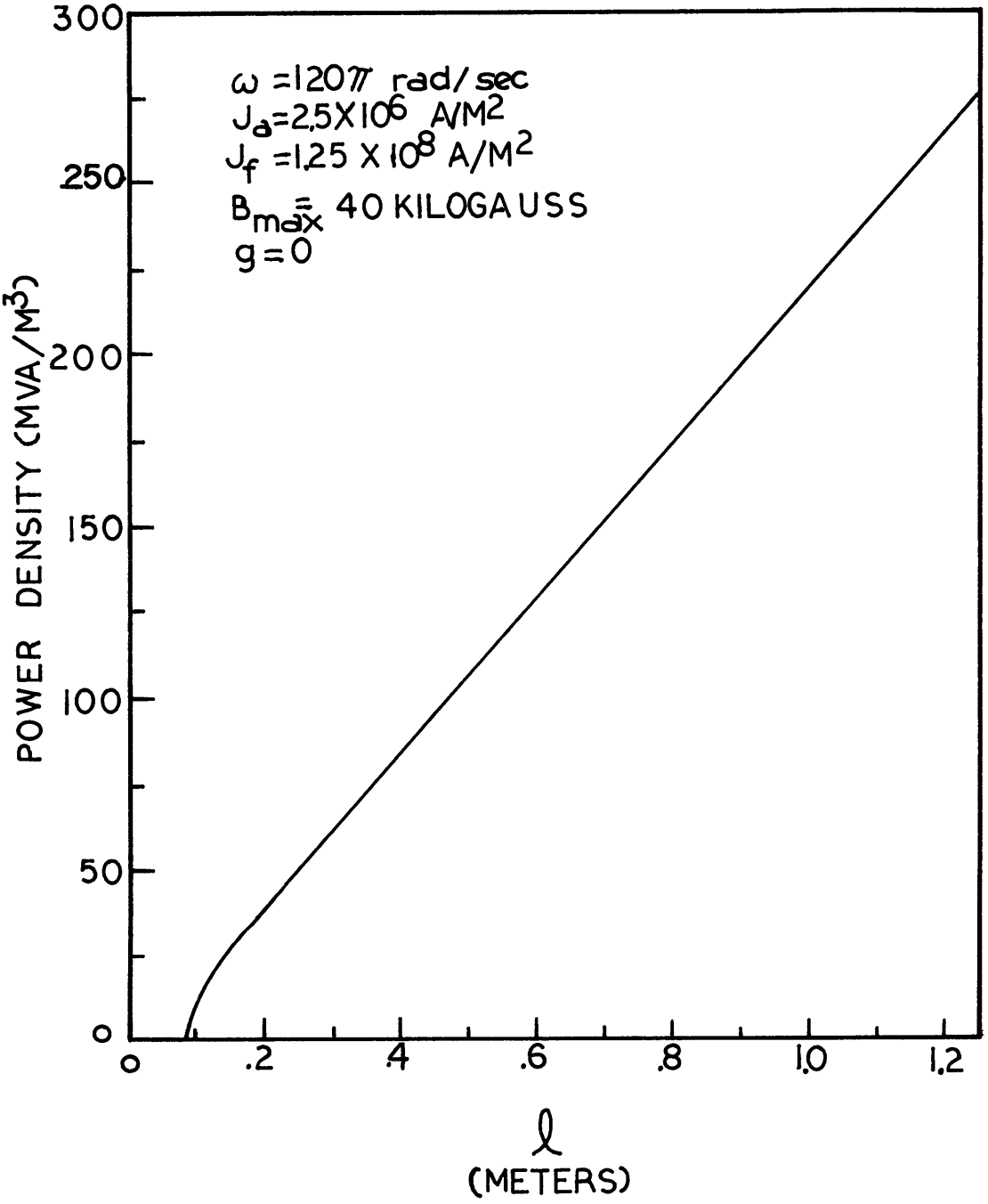

FIG. 7 POWER DENSITY VERSUS POLE PITCH

thickness that gave a ninety percent effectiveness was chosen, i.e. ($t_a = .735\ \ell$). For simplicity, the air gap dimension was assumed to be zero. The characteristic field winding thickness, $\frac{\pi t_f}{\ell}$, that gave a maximum field density of 40 kilogauss, was used. This ratio of field thickness to pole pitch varied with different values of ℓ, but for the large pole pitches it is small compared with the armature thickness to pole pitch ratio ($\frac{t_a}{\ell}$). The power density could then be approximated by:

$$\text{Power Density} \approx \frac{P}{2\ell^2 L_m}$$

Other parameters held constant were the electrical frequency, $\omega_e = 377$ radians/sec, and the current densities, $J_a = 2.5 \times 10^6$ Amps/m^2 and $J_f = 1.25 \times 10^8$ Amps/m^2. Also, no iron shields were used. A family of curves could be plotted by varying any one of these parameters independently of the others. The curve for a conventional machine would have a similar shape but a much smaller slope due to the lower values of field current density that may be used.

The curve is nonlinear at the smaller values of pole pitch because the field thickness to pole pitch ratio is not negligible here. The power density goes to zero at some finite value of pole pitch because the synchronous reactance approaches unity at this value of pole pitch. This is really an artificial situation because X_a can be changed by adjusting the field current to a new value, thereby moving to

a new curve. The approximations and assumptions break down in this lower region, but good approximations of power density can be made from the larger pole pitches in the linear region.

This curve may be used to determine several different parameters of the machine. There are several expressions relating machine parameters which may be used in the approximation of a large cylindrical machine.

$$\ell = \frac{\pi V_{tip}}{\omega_e}, \qquad \ell = \frac{\pi R}{p}, \qquad V_{tip} = \omega_m R$$

With these relations and the pole pitch versus power density curve (Figure 7) we can determine the machine dimensions. Usually the electrical frequency, ω_e, at which the machine will be operated is known. Also, the mechanical speed is known from the speed requirements of the load. These two frequencies then will determine the number of the poles required on the motor. If a tip speed is known, this, along with the mechanical speed, will fix the rotor diameter and the pole pitch.

We have thus far determined the electrical frequency, rotor speed, tip speed, rotor diameter, number of poles, and the pole pitch. A power density of the machine can then be determined from Figure 7 for the corresponding pole pitch. Thus, an approximate power rating per unit length is determined. This linear analysis demonstrates the ease of deciding machine parameters for a first approximation.

Chapter III. Design of a Motor

With the linear geometry model complete, the next step is the design of a large power rating, multipole, synchronous motor based on this new model. First, however, the validity of the model must be determined. The accuracy of the linear expressions for the field intensities and the inductances was checked by taking the limit of the corresponding cylindrical geometry expressions as the number of pole pairs and the radius approach infinity.[1] By careful use of power series expansions it can be shown that;

$$\lim_{\substack{p \to \infty \\ R \to \infty}} L(r,\theta) = L(x,y) \qquad \lim_{\substack{p \to \infty \\ R \to \infty}} H(r,\theta) = H(x,y)$$

This limit-taking process is done in Appendix B.

Once the accuracy of the expressions has been checked, it must be shown that they are good approximations of the cylindrical expressions for multipole machine designs. This can be done by comparing the power rating expressions over a range of pole pairs. The results of this analysis are shown in Figure 8 where the ratio of the flat power rating to the cylindrical power rating is plotted versus pole pairs.

To actually compare the two expressions numerically, certain parameters were fixed. A family of such curves can be plotted by changing one of the independent parameters. For this study the speed was chosen as 75 feet per second

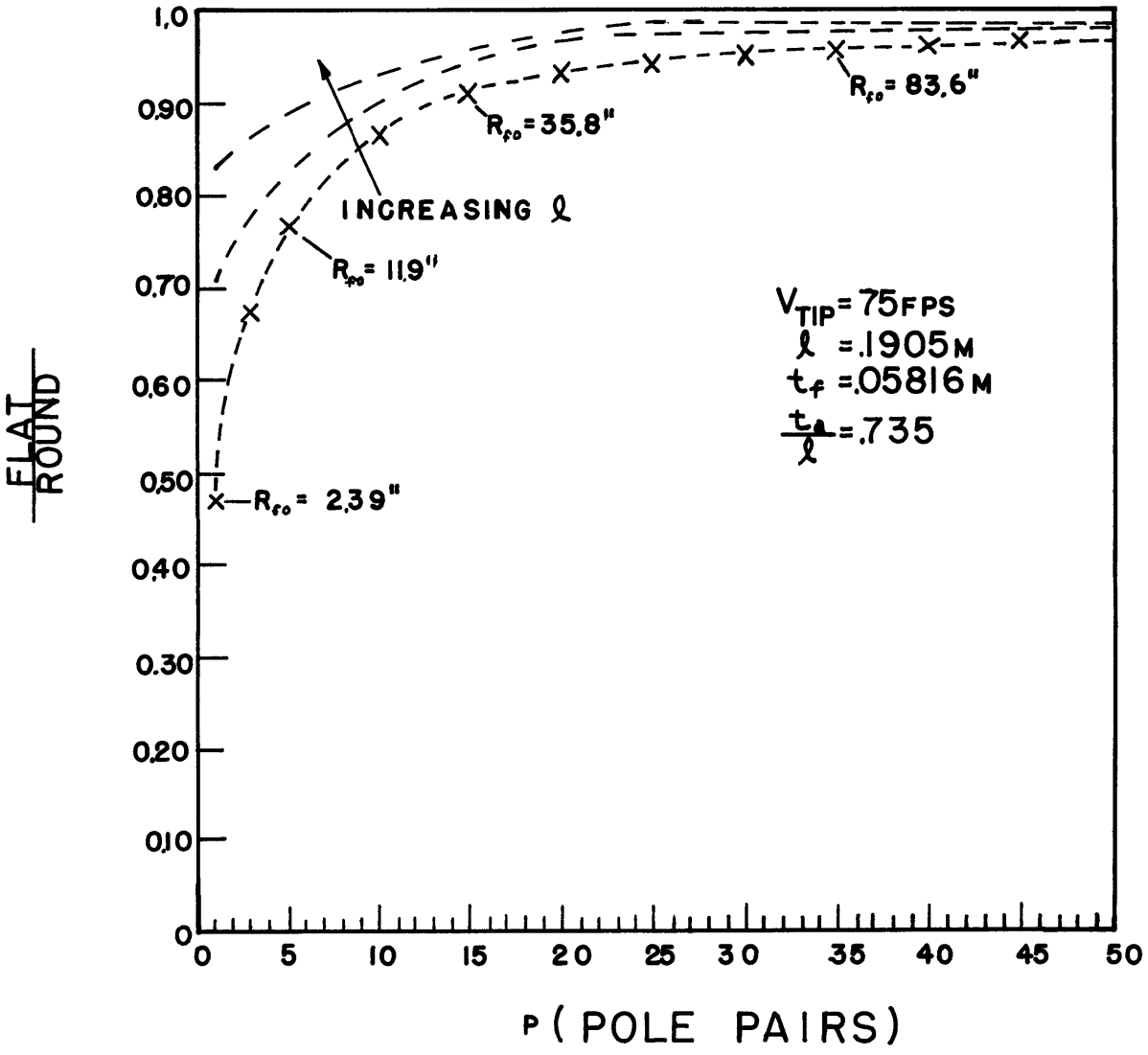

FIG. 8 POWER RATING RATIO VERSUS POLE PAIRS

which is to be on the linear portion of the power density vs. pole pitch curve, Figure 7. The electrical frequency was fixed at 60 hertz. These two parameters, then, fixed the pole pitch, ℓ, at .1905 meters (7.5 inches). To maintain a constant pole pitch, the diameters of the machine had to vary directly proportional to the number of pole pairs. In Figure 8, as we move to a higher number of pole pairs, we get increasingly larger diameter machines.

$$R_m = \frac{p\ell}{\pi} \qquad \text{where } R_m = (R_{fi} + t_f/2) = (R_{fo} - t_f/2)$$

The armature thickness, t_a, was chosen from Figure 6 to yield a ninety percent effective armature. The field winding thickness, t_f, gives a maximum field flux density of 1.25×10^8 A/m^2. The air gap dimension, g, was arbitrarily chosen as one inch. Effects due to iron shields were neglected, and V_t/E_f was held constant at unity.

The results of this analysis were consistent with the results of the limiting case of the cylindrical expressions. The linear analogy yields poor results for small diameter machines with a low number of pole pairs, but rises asymptotically to unity as the pole pair number and machine diameter approach infinity. This plot indicates that simplified linear power rating expressions give results of ninety percent accuracy for machines with fourteen pole pairs, a pole pitch of 7.5" and a radius of 33.4". The conclusion is drawn that a linear analysis

yields a good approximation of large diameter, multipole, cylindrical machines.

Motor Design

The linear analysis is now used to design a large, superconducting, propulsion motor. The motor is required to match the performance of a conventional synchronous motor proposed by the General Electric Co. for an electric ship propulsion system with gas turbine prime movers and speed control by varying prime mover speed. Comparisons of the two designs can then be made.

The motor is required to have a power rating of 40,000 horsepower (29.82 MW) at a shaft speed of 120 revolutions per minute. Gas turbine design speed is 3600 revolutions per minute. The direct coupled synchronous generator is a two pole, 60 hertz machine. This requires 60 poles on the motor for sychronous speed reduction to 120 r.p.m. The three steps of the design procedure are: 1) determine primary machine dimensions from the linear expressions for the initial design; 2) utilize the dimensions determined in step one in the cylindrical expressions for the actual machine design; and 3) compare the superconducting machine design with the conventional design. Table IV lists the machine parameters determined from step one and step two. In the linear analysis the tip speed of seventy-five feet per second was chosen from the linear portion of Figure 7.

The tip speed, along with the electrical frequency, determine the pole pitch. The pole pitch and the pole pair number determine a mean radius (R_m).

$$R_m = \frac{p\ell}{\pi}$$

The superconducting machine in this design has a maximum field of 40 kilogauss in the winding with a field current density of 1.25×10^8 A/m^2. This requires the field winding to be 2.29 inches thick. An air gap dimension of one inch was chosen to allow for mechanical support structure and an electro-thermal damper shield. A magnetic iron shield was positioned just behind the armature winding. The minimum thickness required is determined from $B_{max} \leq B_{saturation}$ within the magnetic shield. Saturation of iron occurs at a flux density of about 15 kilogauss. An armature current density of 2.5×10^6 Amp/m^2 is assumed. All of these parameters can be then used in the power rating expression to determine the straight section length required to produce 29.82 megawatts.

With these parameters determined, the equivalent dimensions were substituted into the cylindrical power rating expression. A new machine length, shorter than the flat rating length, was calculated. Results are listed in Table IV .

Step three of this procedure entails a comparison of this new superconducting motor design with a conventional motor design for similar performance requirements.

TABLE IV

Electrical and Mechanical Machine Parameters

	Linear	Cylindrical
Power Rating: P	40,000 HP (29.82MW)	40,000 HP (29.82 MW)
Shaft Speed: N	120 R.P.M.	120 R.P.M.
Electrical Frequency: ω_e	60 Hertz	60 Hertz
Power Factor: cos ψ	1.0	1.0
Number of Poles: 2p	60	60
Rotor Tip Speed: V_{tip}	75 fps	75 fps
Pole Pitch: ℓ	7.5 inches	7.5 inches
Field Winding Thickness: t_f	2.29 inches	2.29 inches
Armature Winding Thickness: t_a	5.56 inches	5.56 inches
Air Gap Dimension: g	1.0 inch	1.0 inch
Inside Field Radius: R_{fi}		69.23 inches
Outside Field Radius: R_{fo}		71.52 inches
Inside Armature Radius: R_{ai}		72.52 inches
Outside Armature Radius: R_{ao}		78.08 inches
Magnetic Shield Radius: R_s		78.08 inches
Magnetic Shield Thickness: t_s	1.35 inch	1.35 inch
Armature Radius Ratio: X		.9293
Field Radius Ratio: Y		.9680
Maximum Field in Winding: B_{max}	40 kilogauss	
Effective Length: L_m	.52855m 20.81 in.	
Synchronous Reactance: x_a (Normalized to E_f)	.189	.27
Armature Current Density: J_a	2.5×10^6 Amp/m^2	2.5×10^6 Amp/m^2
Field Current Density: J_f	1.25×10^8 Amp/m^2	1.25×10^8 Amp/m^2

FIG. 9 COMPARATIVE MOTOR SIZES
SIDE VIEW

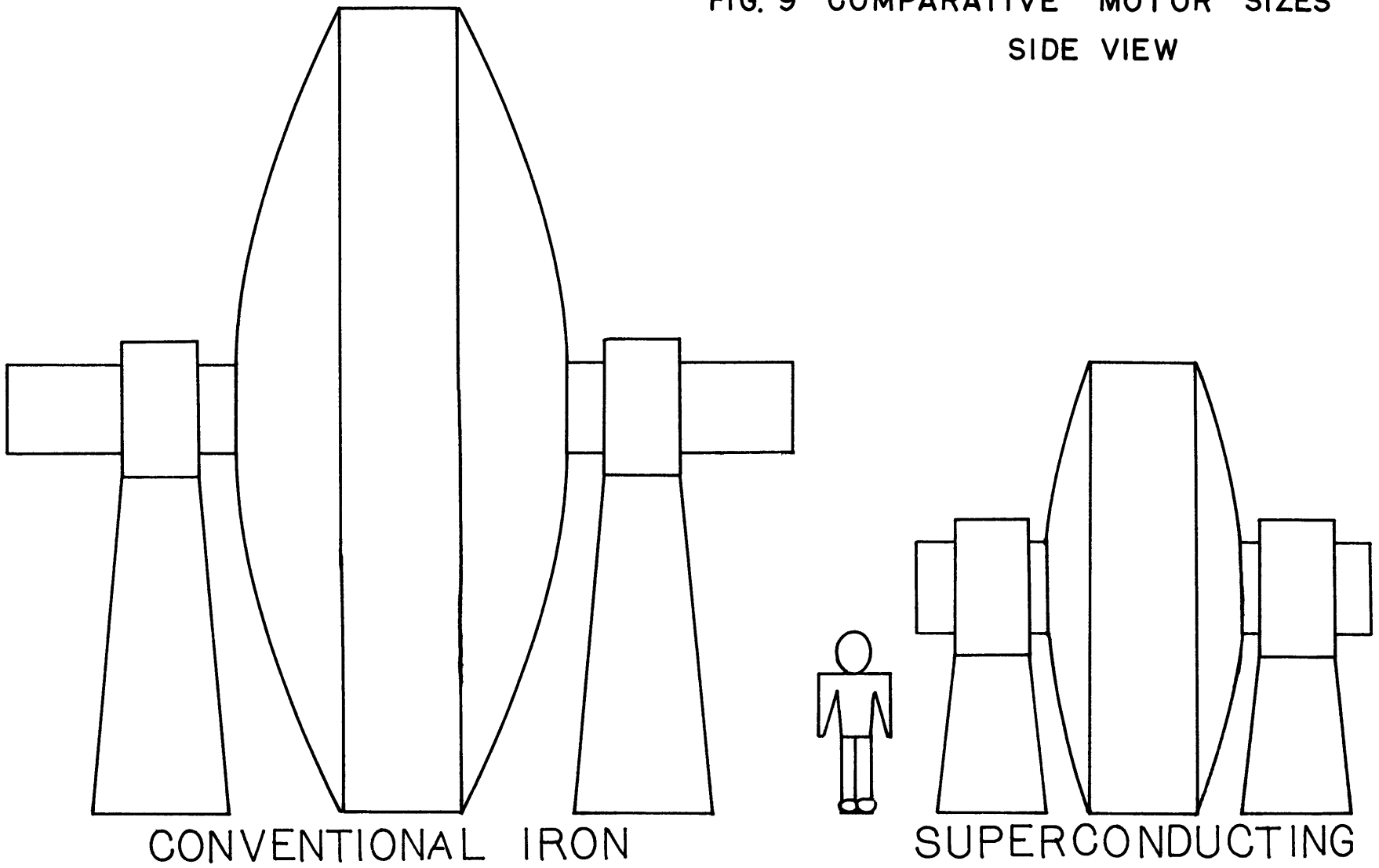

FIG. 10 COMPARATIVE MOTOR SIZES
END VIEW

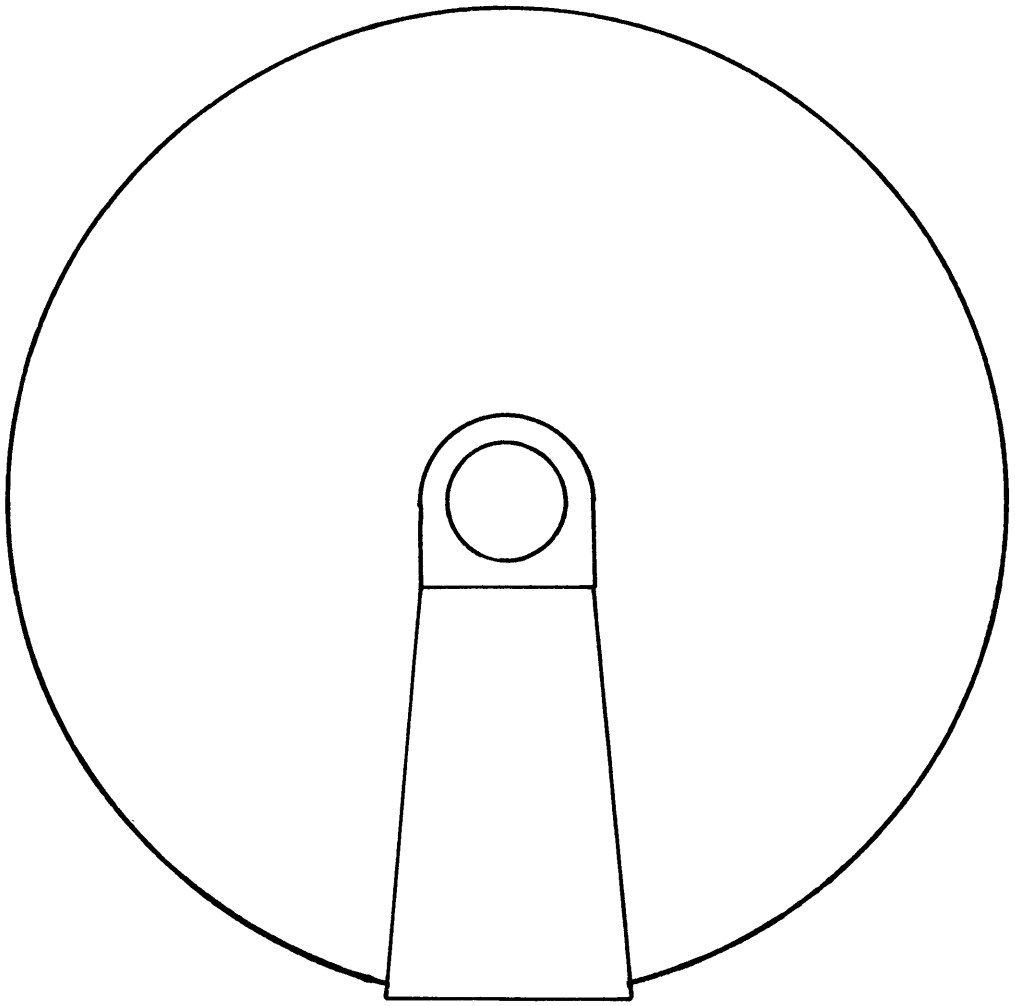

CONVENTIONAL IRON

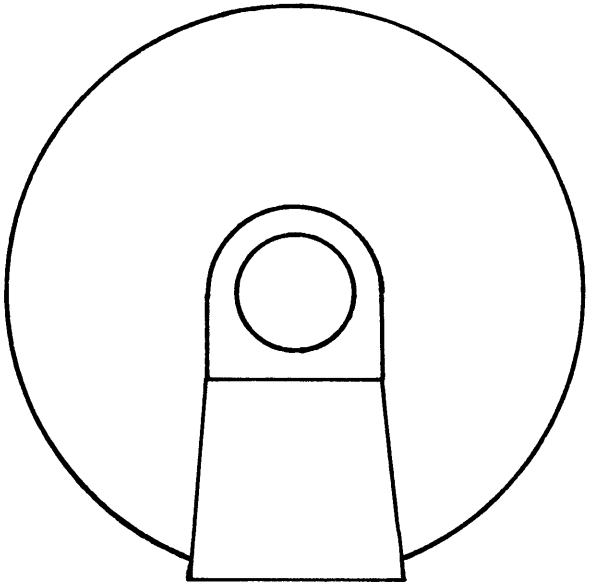

SUPERCONDUCTING

The General Electric Company has a design for a 40,000 HP, 60 pole, 120 R.P.M. synchronous motor for a ship propulsion system. Exact electrical and mechanical parameters are not available, but overall physical size can be compared with the superconducting design. The conventional motor has an overall outside diameter of twenty-six (26) feet compared with fifteen (15) feet for the superconducting design. The rotor lengths are of about equal dimensions; approximately four (4) feet. Figures 9 and 10 demonstrate the approximate physical sizes and the significant increase in power density that can be obtained with superconducting machinery.

Another conventional propulsion motor design by the General Electric Company has approximately the same physical dimensions as this superconducting design. It is a 72 pole, 100 R.P.M., unity power factor, synchronous motor, but has a power rating of only 12,500 horsepower.

The comparison of the superconducting motor dimensions from this design with the large propulsion motors of the General Electric Company demonstrates explicitly the advantage of superconducting machinery in power density increases. By this analysis, a size reduction of approximately one-half is possible by use of superconductors.

A simple method of comparing all rotating electric machines of varying dimensions, speed, and power ratings, is by means of the average air gap magnetic shear stress (σ_m).

TABLE V

Comparison of Magnetic Shear Stress Levels for Various Superconducting and Conventional Electric Machines

Machine Description	Power Rating P(KW)	Mechanical Frequency ω_m	Rotor Diameter D(in.)	Rotor Length L(in.)	σ_m(PSI)
1) AVCO, S.C. operating	8	1257	2.18	4.49	1.68
2) First MIT S.C. oper.	80	377	5.75	4.5	7.76
3) USSR S.C. operating	62	314	5.51	9.84	3.72
4) USSR S.C. operating	1×10^3	157	20.3	21.4	4.07
5) Second MIT S.C. oper.	2×10^3	377	8.0	24.0	19.47
6) Westinghouse S.C. oper.	5×10^3	377	10.2	17.6	40.81
6') Proj. capability w/ mod.	1.5×10^4	377	10.2	17.6	147
7) Westinghouse S.C. Ship Drive Design	3×10^4	18.85	87.25	27.0	43.4
8) MIT Design of Thesis	3×10^4	12.57	143.04	20.0	31.0
9) IRD, S.C. Paper design	5×10^5	377	41.3	145.0	36.29
10) MIT, S.C. Paper design	1×10^6	377	35.2	123.3	97.7
11) G.E., S.C. Paper design	2×10^6	377	43.0	117.5	98
12) MIT, S.C. IEEE Paper design	1×10^6	377	21.6	130.0	246.4
13) G.E. Ship Drive Motor Conventional	3×10^4	12.57	240	48	4.86
14) Westinghouse Airborne S.C. Operational	5×10^3	1257	10	10.5	20.38

TABLE V

(Continued)

Machine Description	Power Rating P(KW)	Mechanical Frequency m	Rotor Diameter D(in.)	Rotor Length L(in.)	$_m$(PSI)
15)Various conventional alternators, operating, mostly on AEP system:					
(1964)	3×10^5	377	37.0	200.0	16.4
(1953)	4.4×10^4	377	29.0	125.0	6.26
(1953)	1.12×10^5	188.5	54.0	167.0	6.87
(1953)	1.47×10^5	377	38.0	180.0	8.45
(1953)	1.25×10^5	188.5	56.0	150.0	8.00
(1970)	8.0×10^5	377	44.5	290.0	20.82
(1970)	8.0×10^5	377	43.0	245.0	26.4
	1.30×10^5	377	40.0	179.0	6.79

FIG. 11 MAGNETIC SHEAR STRESS VERSUS MACHINE RATING

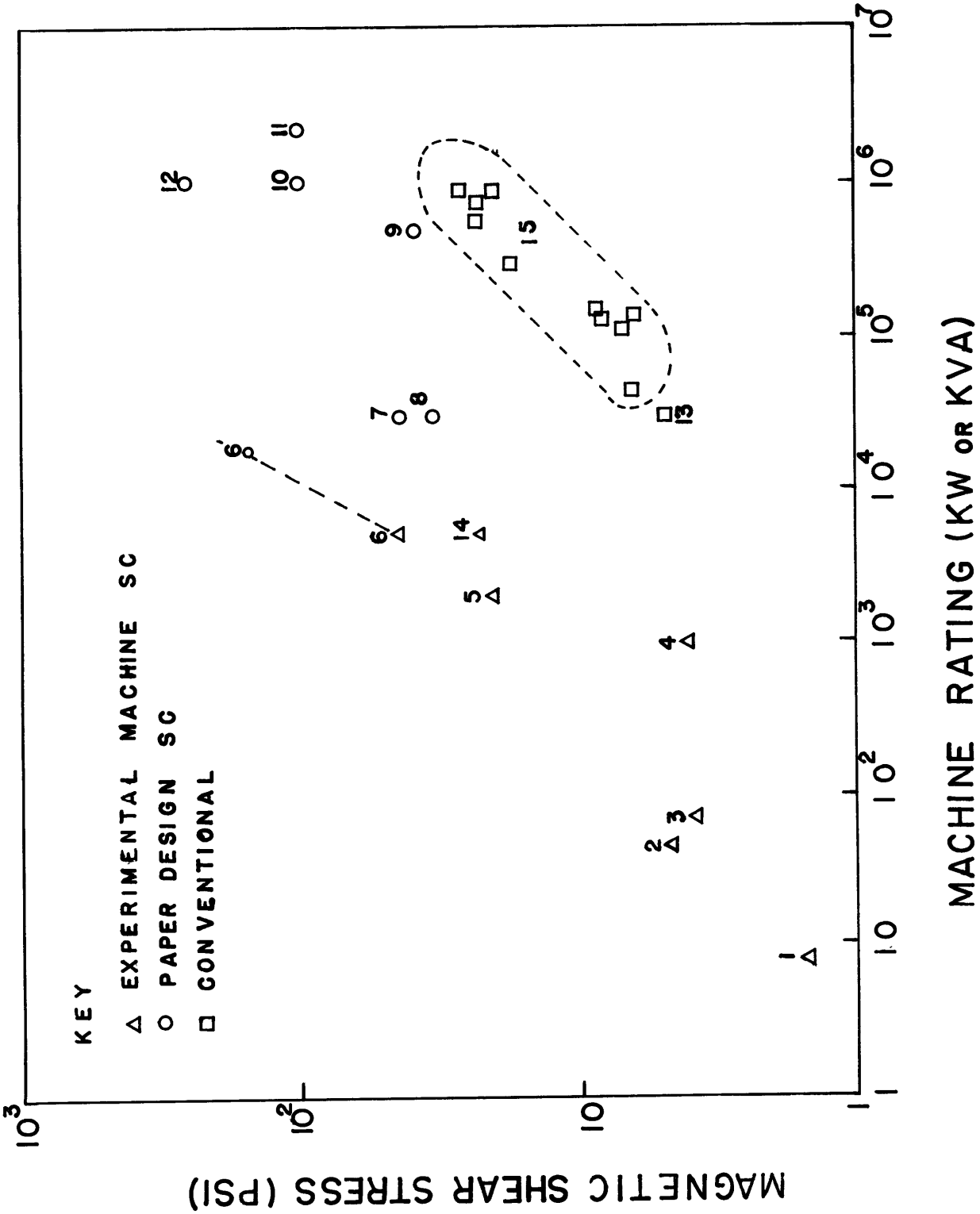

It is a measure of the machine size and the average magnetic power transmitted across the air gap. It can be calculated from the power rating and the machine dimensions.

$$P = T\omega_m$$

$$T = (\text{shear stress})(\text{surface area})(\text{radius}) = (\sigma_m)(\pi DL)(\frac{D}{2})$$

$$\sigma_m = \frac{2P}{\pi D^2 L \omega_m}$$

This gives a quite simple measure of power per unit volume. A survey of various conventional and superconducting electric machines has been made, including both machines already in operation and proposed paper designs. These results are listed in Table V and the corresponding values of magnetic shear stress versus machine rating are plotted on a log-log scale in Figure 11. This figure exhibits basically an exponential growth in achievable shear stress levels with increases in magnetic shear stress of up to approximately an order of magnitude by superconducting machines over conventional designs.

Chapter IV: Motor Starting

An important requirement in the design of a synchronous motor is that it possess the ability to start itself by induction motor action. This can be accomplished with short-circuited damper or amortisseur bars imbedded in the field pole faces to form a squirrel cage rotor. A cylindrical copper damper shield also serves the same purpose. With the unexcited field winding circuit closed through a large resistance the motor should approach synchronous speed by induction motor action. Then, when the external resistance is removed from the field winding circuit, and the field is excited, the rotor should pull into synchronism with the armature field.

In a synchronous system for ship propulsion this is difficult because the motor must be started under load, directly coupled to the propeller. During maneuvering operations the motor must be capable of being repeatedly brought up to about one quarter of full speed ahead or astern and then synchronized, without excessive rotor heating. It would not be feasible to bring the speed of the motor up from zero with the field energized by raising the gas turbine speed, because the turbine has a minimum idling speed.

This motor design utilizes a cylindrical conducting copper shield for induction motor starting and for use as an electrical damper winding during machine transients and

faults. An analysis of this damper shield was done to determine its induction starting capabilities and its ability to be pulled into step. The analysis consists of three parts. The first step involves the solution of the fields created by the armature winding and the induced asynchronous currents in the damper shield during starting. These fields are then utilized in part two to solve for the magnetic forces on the shield by application of Maxwell's stress tensor. These forces can then be converted into a torque-speed characteristic curve to analyze the motor's induction starting capability. The third part of the analysis is to determine whether or not the rotor will pull into synchronism when the field is energized.

Solution of the Magnetic Fields

The damper shield can be modelled as a flat sheet with surface conductivity σ_s permeability μ_o and moving with velocity V. The armature is modelled as a flat traveling wave of surface current $\bar{K}$;

$$\bar{K} = K \cos(\omega_s t - kx)\bar{i}_z$$

where ω_s is the synchronous frequency of the armature currents and k is the wave number. There is no contribution to the magnetic fields from the field winding because it is unenergized and short circuited through a large external resistance during starting. Figure 12 shows the geometric configuration of the flat model.

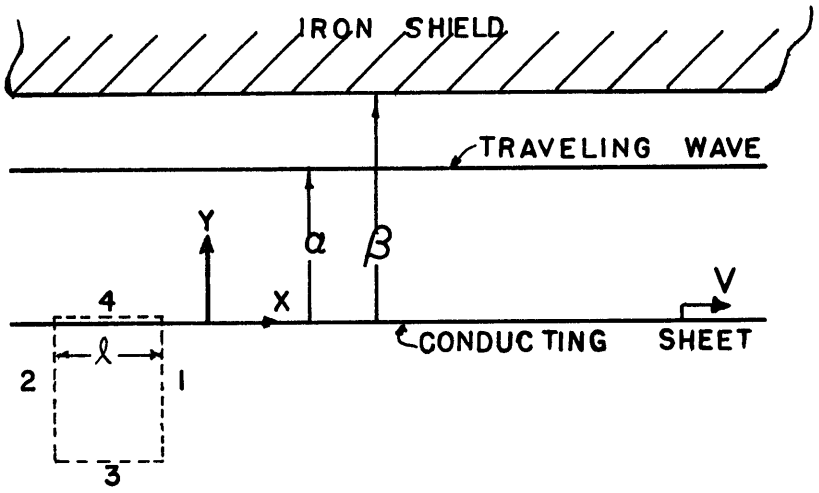

FIG. 12 CONFIGURATION FOR SOLUTION OF FIELDS AROUND DAMPER SHIELD

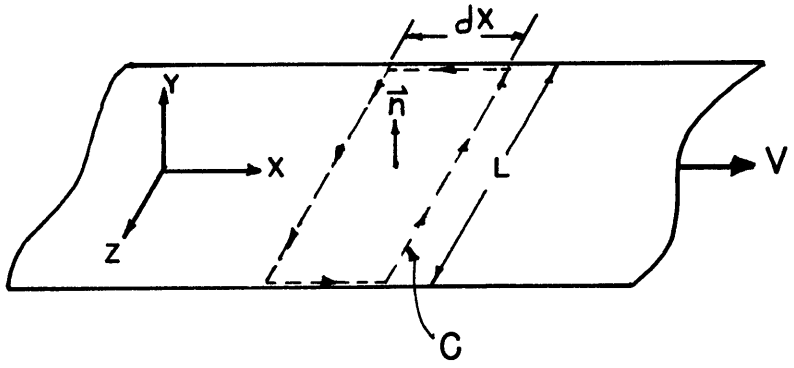

FIG. 13 CONTOUR FOR CALCULATION OF $\vec{E}$ FIELD

We must solve for the $\overline{B}$ fields in the three regions a) between the armature and the upper iron boundary; b) between the armature and the shield; and c) below the shield. One other unknown is $\overline{K}_f$, the induced current in the moving shield conducting sheet. Maxwell's equations give us governing equations which apply in the three current-free regions, a, b, and c.

$$\nabla X\overline{H} = o \qquad \text{and } \nabla\cdot\overline{B} = o$$

We know one other constitutive relation from the application of Ohm's Law in the moving current sheet:

$$K_f' = \sigma_s E'$$

Primes denote quantities measured in the moving frame. With the field transformations this becomes:

$$\overline{K}_f = \sigma_s(\overline{E} + \overline{V}x\overline{B})$$
$$\overline{K}_f' = \overline{K}_f$$
$$\overline{E}' = (\overline{E} + \overline{V}x\overline{B})$$

Now we can write $\overline{H}$ as the gradient of a scalar potential Φ.

$$H = -\nabla\Phi$$

Therefore, Laplace's equation applies in the three regions.

$$\nabla^2\Phi = 0$$

We can assume variable separable solutions of the form,

$$\Phi = X(x)Y(y)T(t).$$

In this analysis we assume there are no variations in the z direction. We also assume the time varying part of the solution has the same form as the time part of the driving function,

$$T(t) = A \cos \omega_s t + B \sin \omega_s t$$

By substitution into Laplace's equation, the form of the solution for $\bar{H}$ then becomes:

$$\bar{H}_x = k\{(c_1e^{ky}+c_2e^{-ky})\cos\omega_s t \sin kx - (c_3e^{ky}+c_4e^{-ky})\sin\omega_s t\cos kx + (c_5e^{ky}+c_6e^{-ky})\sin\omega_s t\sin kx - (c_7e^{ky}+c_8e^{-ky})\cos\omega_s t\cos kx\}\bar{i}_x$$

$$\bar{H}_y = k\{(c_1e^{ky}-c_2e^{-ky})\cos\omega_s t \sin kx - (c_3e^{ky}+c_4e^{-ky})\sin\omega_s t\cos kx + (c_7e^{ky}-c_6e^{-ky})\sin\omega_s t\cos kx + (c_7e^{ky}-c_8e^{-ky})\cos\omega_s t\sin kx\}\bar{i}_y$$

The boundary conditions that must be satisfied are:

1) at $y = \beta$

$$H_x^a = 0$$

2) at $y = \alpha$

$$\bar{n}x(\bar{H}^a - \bar{H}^b) = \bar{K}$$

$$\bar{H}_x^a - \bar{H}_x^b = -\bar{K}$$

3) at $y = \alpha$

$$\bar{n} \cdot (\bar{B}^a - \bar{B}^b) = 0$$

$$H_y^a - H_y^b$$

4) at $y = 0$

$$\bar{n} \times (\bar{H}^b - \bar{H}^c) = \bar{K}_f$$

$$H_x^b - H_x^c = -K_f$$

5) at $y = 0$

$$\bar{n} \cdot (\bar{B}^b - \bar{B}^c) = 0$$

$$H_y^b = H_y^c$$

6) at $y = -\infty$

$$\bar{H}^c = 0$$

One other equation is necessary to complete the solution. When applying Ohm's law on the moving current sheet we must carefully apply the integral form of Maxwell's equation to determine the $\bar{E}$ field on the sheet.

Choose a contour c in the fixed reference frame with the current sheet moving through the contour.(see Figure 13). The contour bounds an area length L in the z direction and differential width, dx, in the x direction. Assume components of the $\bar{E}$ field in the z direction only as we assume that currents only flow axially (z direction) in this analysis.

$$\oint_c \bar{E}\cdot d\bar{\ell} = -\frac{d}{dt}\int_s \bar{B}\cdot\bar{n}\, da$$

$$E_z L - (E_z + \frac{\partial E_z}{\partial x} dx)L = -\frac{d}{dt}(B_y\, dx\, L)$$

$$\frac{\partial E_z}{\partial x} = \frac{dB_y}{dt}$$

Integrating this, we get:

$$E_z = \int \frac{dB_y}{dt}\, dx$$

Ohm's Law at y ⁓ 0 becomes:

$$\bar{K}_f = \sigma_s\left[\int\left(\frac{dB_y}{dt}\right)dx\bar{i}_z + VB_y\bar{i}_z\right]$$

We can now solve for the unknown constants in each of the three regions. These operations are quite involved. The constants for regions b and c are listed in Table VI in their full form. These may be simplified further by

TABLE VI

$$C_1^b = -\{\frac{K(e^{k(\alpha-2\beta)}+e^{-k\alpha})[(\mu_o\sigma_s)(1+e^{-2k\beta})(\omega_s-kV)]}{[4k^2+(\mu_o\sigma_s)^2(1+e^{-2k\beta})^2(\omega_s-kV)^2]}\}$$

$$C_2^b = \{\frac{K(e^{k(\alpha-2\beta)}+e^{-k\alpha})[(\mu_o\sigma_s)(1+e^{-2k\beta})(\omega_s-kV)}{(1+e^{-2k\beta})[4k^2+(\mu_o\sigma_s)^2(1+e^{-2k\beta})^2(\omega_s-kV)^2]}\}$$

$$C_3^b = -\{\frac{K(e^{k(\alpha-2\beta)}+e^{-k\alpha})[(\mu_o\sigma_s)(1+e^{-2k\beta})(\omega_s-kV)]}{[4k^2+(\mu_o\sigma_s)^2(1+e^{-2k\beta})^2(\omega_s-kV)^2]}\}$$

$$C_4^b = \{\frac{K(e^{k(\alpha-2\beta)}+e^{k\beta})[(\mu_o\sigma_s)(1+e^{-2k\beta})(\omega_s-kV)]}{(1+e^{-2k\beta})[4k^2+(\mu_o\sigma_s)^2(1+e^{-2k\beta})^2(\omega_s-kV)^2]}\}$$

$$C_5^b = \{\frac{K(e^{k(\alpha-2\beta)}+e^{-k\alpha})[4k^2(1+e^{-2k\beta})+(\mu_o\sigma_s)^2(1+e^{-2k\beta})^2(\omega_s-kV)^2]}{2k(1+e^{-2k\beta})[4k^2+(\mu_o\sigma_s)^2(1+e^{-2k\beta})^2(\omega_s-kV)^2]}\}$$

$$C_6^b = \{\frac{K(e^{k(\alpha-2\beta)}-e^{-k\alpha})[(\mu_o\sigma_s)^2(1+e^{-2k\beta})^2(\omega_s-kV)^2]}{2k(1+e^{-2k\beta})[4k^2+(\mu_o\sigma_s)^2(1+e^{-2k\beta})^2(\omega_s-kV)^2]}\}$$

$$C_7^b = -\{\frac{K(e^{k(\alpha-2\beta)}+e^{-k\alpha})[4k^2(1+e^{-2k\beta})+(\mu_o\sigma_s)^2(1+e^{-2k\beta})^2(\omega_s-kV)^2]}{2k(1+e^{-2k\beta})[4k^2+(\mu_o\sigma_s)^2(1+e^{-2k\beta})^2(\omega_s-kV)^2]}\}$$

$$C_8^b = -\{\frac{K(e^{k(\alpha-2\beta)}+e^{-k\alpha})[(\mu_o\sigma_s)^2(1+e^{-2k\beta})^2(\omega_s-kV)^2]}{2k(1+e^{-2k\beta})[4k^2+(\mu_o\sigma_s)^2(1+e^{-2k\beta})^2(\omega_s-kV)^2]}\}$$

TABLE VI

(Continued)

$$C_1^c = -\left\{\frac{K(e^{k(\alpha-2\beta)}+e^{-k\alpha})[(\mu_o\sigma_s)(1+e^{-2k\beta})(\omega_s-kV)]}{[4k^2+(\mu_o\sigma_s)^2(1+e^{-2k\beta})^2(\omega_s-kV)^2]}\right\}$$

$$C_2^c = 0$$

$$C_3^c = -\left\{\frac{K(e^{k(\alpha-2\beta)}+e^{-k\alpha})[(\mu_o\sigma_s)(1+e^{-2k\beta})(\omega_s-kV)]}{[4k^2+(\mu_o\sigma_s)^2(1+e^{-2k\beta})^2(\omega_s-kV)^2]}\right\}$$

$$C_4^c = 0$$

$$C_5^c = \left\{\frac{2kK(e^{k(\alpha-2\beta)}+e^{-k\alpha})}{[4k^2+(\mu_o\sigma_s)^2(1+e^{-2k\beta})^2(\omega_s-kV)^2]}\right\}$$

$$C_6^c = 0$$

$$C_7^c = -\left\{\frac{2kK(e^{k(\alpha-2\beta)}+e^{-k\alpha})}{[4k^2+(\mu_o\sigma_s)^2(1+e^{-2k\beta})^2(\omega_s-kV)^2]}\right\}$$

$$C_8^c = 0$$

TABLE VII

$0 < y < \alpha$

$$\vec{H}_x^{\,b} = \{\frac{2kKe^{-k\alpha}S}{4k^2+S^2}\sinh(ky)\sin(\omega_s t - kx) + \frac{K}{2}e^{-k\alpha}[e^{ky} + \frac{S^2e^{-ky}}{4k^2+S^2}]\cos(\omega_s t - kx)\}\vec{i}_x$$

$$\vec{H}_y^{\,b} = \{\frac{2kKe^{-k\alpha}S}{4k^2+S^2}\cosh(ky)\cos(\omega_s t - kx) - \frac{K}{2}e^{-k\alpha}[e^{ky} - \frac{S^2e^{-ky}}{4k^2+S^2}]\sin(\omega_s t - kx)\}\vec{i}_y$$

$y < 0$

$$\vec{H}_x^{\,c} = \{\frac{kKe^{-k\alpha}e^{ky}}{4k^2+S^2}[S\sin(\omega_s t - kx) + 2k\cos(\omega_s t - kx)]\}\vec{i}_x$$

$$\vec{H}_y^{\,c} = \{\frac{kKe^{-k\alpha}e^{ky}}{4k^2+S^2}[S\cos(\omega_s t - kx) - 2k\sin(\omega_s t - kx)]\}\vec{i}_y$$

$$S = (\mu_o\sigma_s)(1+e^{-2k\beta})(\omega_s - kV)$$

No upper iron shield ($\lim \beta \to \infty$)

$$\vec{K}_f = \{\frac{Ke^{-k\alpha}}{4k^2+S^2}[kS\sin(\omega_s t - kx) - S^2\cos(\omega_s t - kx)]\}\vec{i}_z$$

removing the upper iron shield and by defining a slip factor S, where $S = (\mu_o \sigma_s)(1+e^{-2k\beta})(\omega_s - kV)$.

The simplified field expressions are listed in Table VII. The phase velocity of the traveling wave is $\frac{\omega_s}{k}$, and S is zero when the velocity V of the conductor is equal to the phase velocity. At this velocity, the rotor is moving in synchronism with the armature field, and there are no induced currents in the damper shield. At speeds other than synchronous speed the induced currents have a frequency proportional to the difference in the speeds, $(\omega_s - kV)$.

Figure 14 demonstrates the damping effect of the shield on the magnitude of the magnetic fields. As S approaches zero, the shield speed approaches the phase velocity of the armature wave. When they are in synchronism there are no induced currents in the shield and, therefore, no attenuation of the fields passing through it. As the slip increases the induced currents in the shield increase in an attempt to keep the flux passing through it constant. An important assumption of this model is that the actual shield thickness is less than the skin depth of the material. For this design the shield thickness was chosen to be 0.50 inch, which is less than the skin depth of 0.667 inch. This is the skin depth corresponding to a maximum asynchronous frequency of 94.25 radians/sec during starting.

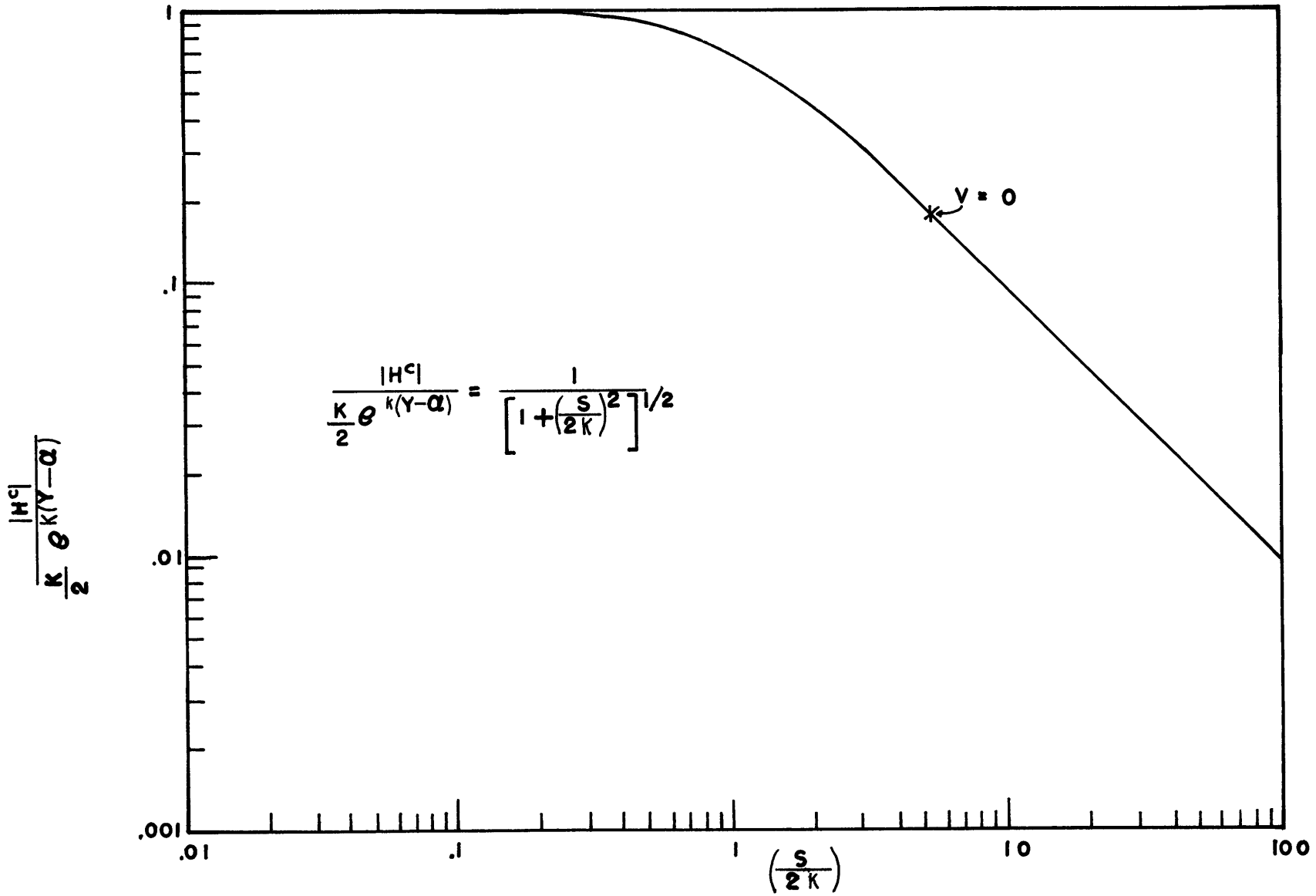

FIG. 14 FIELD ATTENUATION VERSUS SLIP FACTOR

Magnetic Forces on the Damper Shield

With these expressions for the fields surrounding the moving shield we can apply Maxwell's stress tensor to determine the forces of magnetic origin acting upon the shield. Choose a surface that encloses the damper shield as shown in Figure 12. We calculate the force per pole by enclosing one pole with an axial depth L. Surfaces 1 and 2 are $\frac{2\pi}{k}$, one wave length, apart. This is equivalent to encompassing one pole. Surface 3 is very far below the shield where the fields are of zero magnitude. The traction on this surface is zero and contributes nothing to the force's acting on the shield. Surface 4 is at an infinitesimal distance above the shield but in the region b. The tractions on surfaces 1 and 2 are of equal magnitude, being one pole apart, but of opposite direction, therefore cancelling each other. Hence the only contribution to the force is due to the tractions on surface 4. Surfaces 5 and 6 (in the x-z plane) also have tractions of equal magnitudes and opposite direction.

$$f_m = \int T_{mn} n da$$

$$f_x = \int_1 T_{xx} da - \int_2 T_{xx} da + \int_4 T_{xy} da - \int_3 T_{xy} da$$

On surfaces 1 and 2:

$$T_{xx} = \mu_o \left(\frac{H_x^{c2}}{2} + H_y^{c2} \right)$$

On surface 3:

$$T_{xy} = 0$$

On surface 4:

$$T_{xy} = \mu_o H_x{}^b H_y{}^b$$

$$f_x = L \int_o^{2k} \mu_o H_x{}^b H_y{}^b \Big|_{y=o} dx$$

Total force per pole in the x-direction is:

$$f_x = \frac{\mu_o L K^2 \pi S e^{-2k\alpha}}{(4k^2 + S^2)^2} \left[1 + \left(\frac{S^2}{4k^2+S^2}\right)\right]$$

This force can be non-dimensionalized and plotted versus $\frac{S}{k}$ as shown in Figure 15.

$$\frac{fx}{\mu_o \ell L K^2 e^{-2k\alpha}} = \left(\frac{S}{k}\right) \frac{\left[4+2\left(\frac{S}{k}\right)^2\right]}{\left[4 + \left(\frac{S}{k}\right)^2\right]^2}$$

The curve displays typical induction motor characteristics. For starting purposes of this particular machine synchronous speed was chosen to be one-fourth of normal operating speed. For zero rotor speed then, S/k = 5.38.

To determine the motor's capability to start itself as an induction motor it is necessary to plot the torque speed characteristics of the load.[8][10] The intersection of the two curves will determine the asynchronous speed at which the rotor will turn. Certain assumptions were made to determine the torque-speed characteristics of a typical propeller load. The propeller is required to transmit 40,000 horsepower at 120 revolutions per minute. This corresponds to a normal cruising torque of 1.75×10^6 ft.-lbs. The optimum propeller

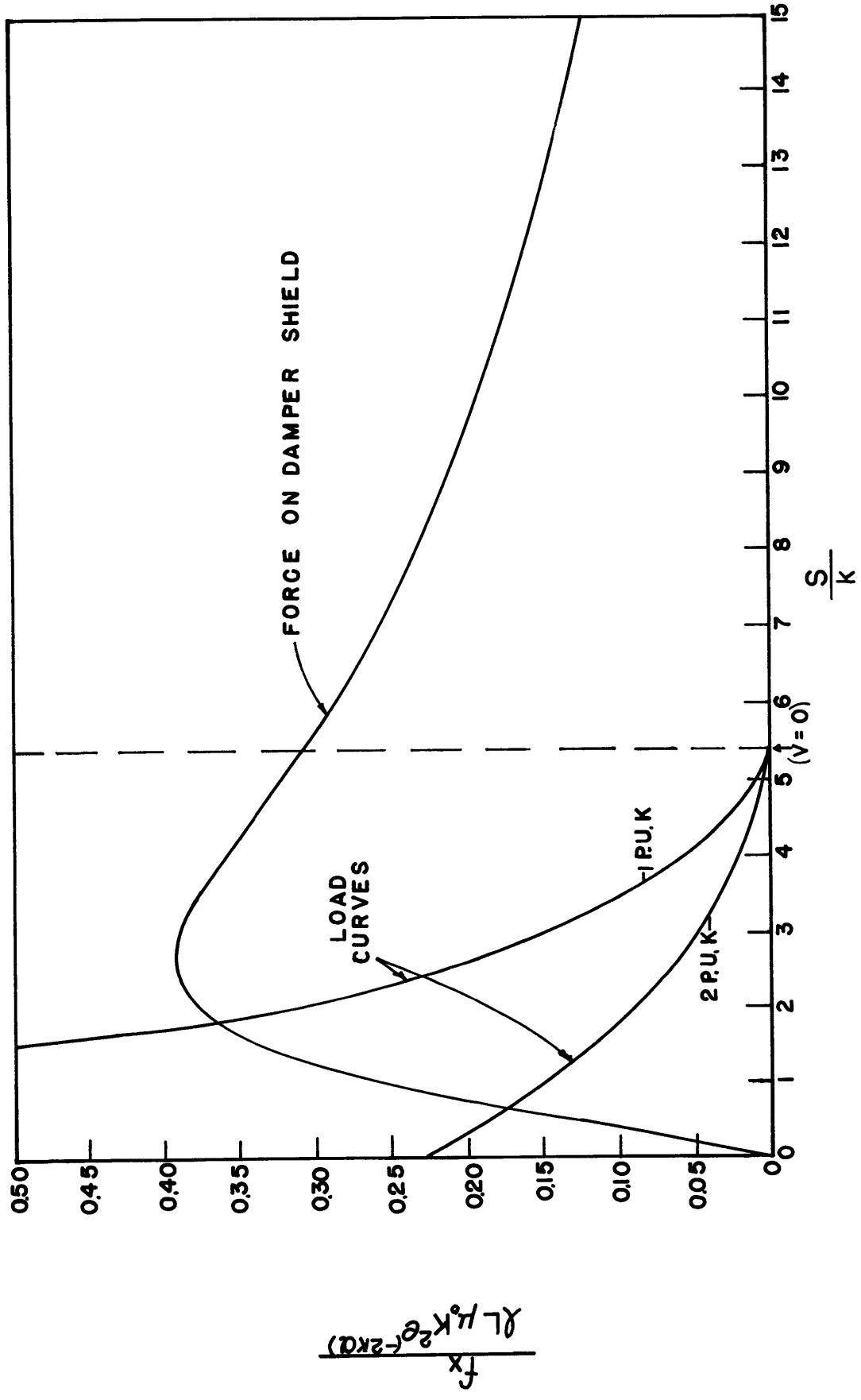

$$\frac{f_x}{\rho L \mu_0 K^2 e^{(-2KQ)}}$$

FIG.15 INDUCTION STARTING FORCES ON DAMPER SHIELD

diameter for this speed and power, 23.5 feet, was computed from the following approximation:

$$D = \frac{(50)(SHP)^{0.2}}{(N)^{0.6}}$$

This may not be the actual propeller diameter that would be used for this ship drive as it neglects many other propeller design parameters such as tip velocity and submergence under water. However, this value was used for a first approximation. Also a normal cruising speed of 17 knots was assumed. The expression relating torque, speed, and propeller diameter is:

$$T = C_Q \rho D^3 (V_p^2 + N^2 D^2)$$

where ρ is the density of sea water (1.94 slugs/ft^3), C_Q is the torque coefficient, and V_p is the speed of advance of the propeller. It is defined by:

$$V_p = (1 - w)V$$

where V is the ship speed and w is the wake ratio,

$$w = (V - V_p)/V$$

The torque coefficient, C_Q, was determined from the operating torque delivered at normal cruising speed and propeller R.P.M. Two values were computed for wake ratios of zero and unity, and the average value was used (C_Q=.0312). A torque-speed curve was then determined over a range of speeds from zero to 30 R.P.M. For this curve, ship speed was assumed to be zero. The curve was then normalized by

the motor rotor radius, number of pole pairs, and the product ($\ell L \mu_o K^2 e^{-2k\alpha}$). The load curve was then superimposed on the induction starting characteristic curve as shown in Figure 15. This was done for starting currents of one per-unit and two per-unit. These values of starting current are conservative. The induction motor action of the damper shield should quickly accelerate the propeller to approximately 26 R.P.M., or 13.5% slip.

Synchronizing

To synchronize the rotor with the armature field, the field winding should be energized at this steady state speed. To determine whether the rotor will be pulled into step it is necessary to know the weight and inertia of the rotor and the inertia of the load. These quantities were not determined in this preliminary electrical study. However, 13.5% slip appears to be a relatively large value of slip from which to synchronize. This can be improved be increasing the stator current. But the problem of shield heating and heat dissipation by rotor cooling must be analyzed. The length of time the motor is run as an induction motor before synchronizing must also be taken into account.

One of many possible methods to synchronize this motor is by performance of the following steps:

1) With the field winding de-energized, bring the rotor

speed up by induction motor action to a value greater than synchronizing speed. If you wish the motor to be synchronized at 30 R.P.M., bring the speed to just over 30 R.P.M. by running the prime mover and the generator at the required speed greater than 900 R.P.M.;

2) Slow the prime mover speed quickly to 900 R.P.M. for a corresponding synchronous frequency of 15 hertz;

3) The motor will begin to slow down. When the rotor is turning at exactly 30 R.P.M., energize the field winding. The motor will now be synchronized.

This type of operation is somewhat delicate and more complicated than a straightforward, conventional synchronizing operation. However, it is a feasible method of insuring motor synchronism without slipping poles. It appears that it is possible to start this motor by induction motor action on the damper shield and synchronize it.

Chapter V. Conclusions

The linear geometry machine proved to be a good model for large diameter, multipole, synchronous electric machines. Field and power rating expressions for flat geometry machines are good approximations of the corresponding cylindrical expressions when applied to large, multipole designs. The flat power rating is approximately 90% of the value determined from the cylindrical power rating for a machine with fourteen (14) pole pairs, a tip speed of 75 feet per second, and a diameter of about 5 1/2 feet.

An important advantage of the flat model over the cylindrical model is the simplicity of the field and power rating expressions in the basic form. The field expressions demonstrate explicitly the field distribution. The results of changing the basic design parameters such as armature thickness, field thickness, and pole face angle, air gap dimension, and field and armature currents, are readily computed. Their effect on the machine power rating gives the designer a relatively simple method of determining good approximate values of these parameters for the initial design.

The significant parameters for machine design are the pole pitch, ℓ, and the dimensionless parameters:

$$\frac{\pi g}{\ell}\ ,\quad \frac{t_f}{\ell}\ ,\quad \frac{t_a}{\ell}\ ,\quad \text{and}\quad \frac{|H|}{\frac{4J_f\ell}{\pi^2}\sin\left(\frac{\pi S_{wf}}{2\ell}\right)}$$

The power rating falls exponentially with an increasing air gap dimension. The machine output is also limited by these

other design parameters. The effective coupling with the armature is demonstrated in Figure 6. With existing superconductors the field current density, and thus machine rating, is limited by the maximum field allowed in the winding. Figures 2 and 3 show these maximum values. From the power density versus pole pitch curve, Figure 7, we can see that, without careful design, a machine may be designed with finite dimensions and zero power output. This could occur when certain design parameters such as field current and armature current densities are chosen at optimum values, but the synchronous reactance causes zero terminal voltage.

This analysis has also shown that large multipole synchronous machines can be designed with significant power density increases over conventional machines. The 29.82 M.W., 60 pole, 120 R.P.M., superconducting motor designed in this study has a diameter of approximately one half that of a conventional electric motor for similar performance requirements.

The analysis of starting the motor on the damper shield by induction motor action has shown that it may be possible to start and synchronize the motor in this fashion. However, in a ship propulsion system where rapid speed and directional changes are common during maneuvering operations, this damper shield will undergo a heavy duty. Further study should be devoted to careful design of the shield and rotor cooling requirements during transients. This coincides with a more detailed analysis of the propeller load to which the motor is coupled.

APPENDIX A

Field Analysis for Linear Geometry

I. Solution of the Magnetic Field

The problem is to solve for the magnetic field distribution in free space due to a linear field winding of finite thickness between two plane parallel magnetic iron boundaries. The first step is to solve the problem for a current sheet between the two iron boundaries and then expand the sheet by superposition into a winding of finite thickness.

First the current sheet is represented as a summation of cosine functions in a Fourier analysis. The current distribution in the current sheet is shown in Figure 16.

$$f(x) = \sum_{n=1}^{\infty} K_n \cos\frac{n\pi x}{\ell}$$

where

$$f(x) = \begin{cases} +K & 0 \leq x < \dfrac{S_w}{2} \\ 0 & \dfrac{S_w}{2} < x < \dfrac{S_w}{2} + b \\ -K & \dfrac{S_w}{2} + b < x \leq \ell \end{cases}$$

K_n is determined from standard Fourier's methods to be

$$K_n = \begin{cases} 0 & n = 2,4,6,8,\ldots \\ \dfrac{4K}{n\pi} \sin\dfrac{n\pi S_w}{\ell} & n = 1,3,5,7,9,\ldots \end{cases}$$

Now the field solutions must be found. The differential forms of Maxwell's equations in current free space are written as: $\nabla \cdot \overline{B} = 0$, $\nabla x \overline{H} = 0$

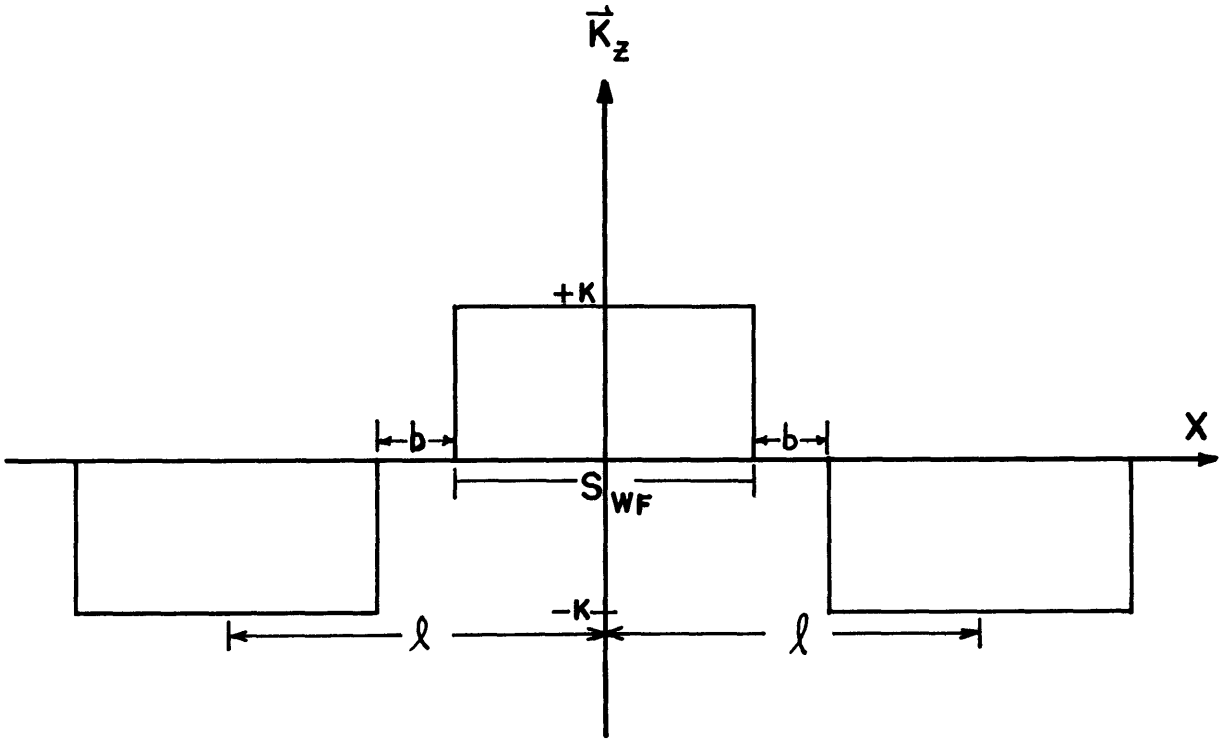

FIG. 16 CURRENT DISTRIBUTION IN CURRENT SHEET

This allows us to define a scalar potential, Φ , such that:

$$\overline{H} = - \nabla\Phi$$

In current-free space, we then have Laplace's equation:

$$\nabla^2 \Phi = 0$$

and, in a linear coordinate system:

$$\frac{\partial^2 \Phi}{\partial x^2} + \frac{\partial^2 \Phi}{\partial y^2} = 0$$

In our two-dimensional model there is no variation of the field in the z direction, i.e. $\frac{\partial}{\partial z} = 0$. Our solution is independent of z. We can assume variable separable solutions.

$$\Phi = X(x)\ Y(y)$$

Therefore,

$$\frac{X''}{X} + \frac{Y''}{Y} = 0 \qquad \text{and } \frac{X''}{X} = -\lambda^2,\ \frac{Y''}{Y} = +\lambda^2$$

These ordinary differential equations have solutions of the form:

$$X = A \cos \lambda x + B \sin \lambda x \qquad Y = Ce^{\lambda y} + De^{-\lambda y}$$

where $\lambda = \frac{n\pi}{\ell}$

$$\Phi = (C_1 e^{\lambda y} + C_2 e^{-\lambda y})\cos \lambda x + (C_3 e^{\lambda y} + C_4 e^{-\lambda y})\sin \lambda x$$

Figure 17 shows the geometric configuration of the current sheet and the magnetic boundaries. Our solutions must hold for two regions, one between the current sheet and the upper iron boundary, and the other between the current sheet and the lower iron boundary. Boundary conditions must be given for these two regions at the iron boundaries and at the

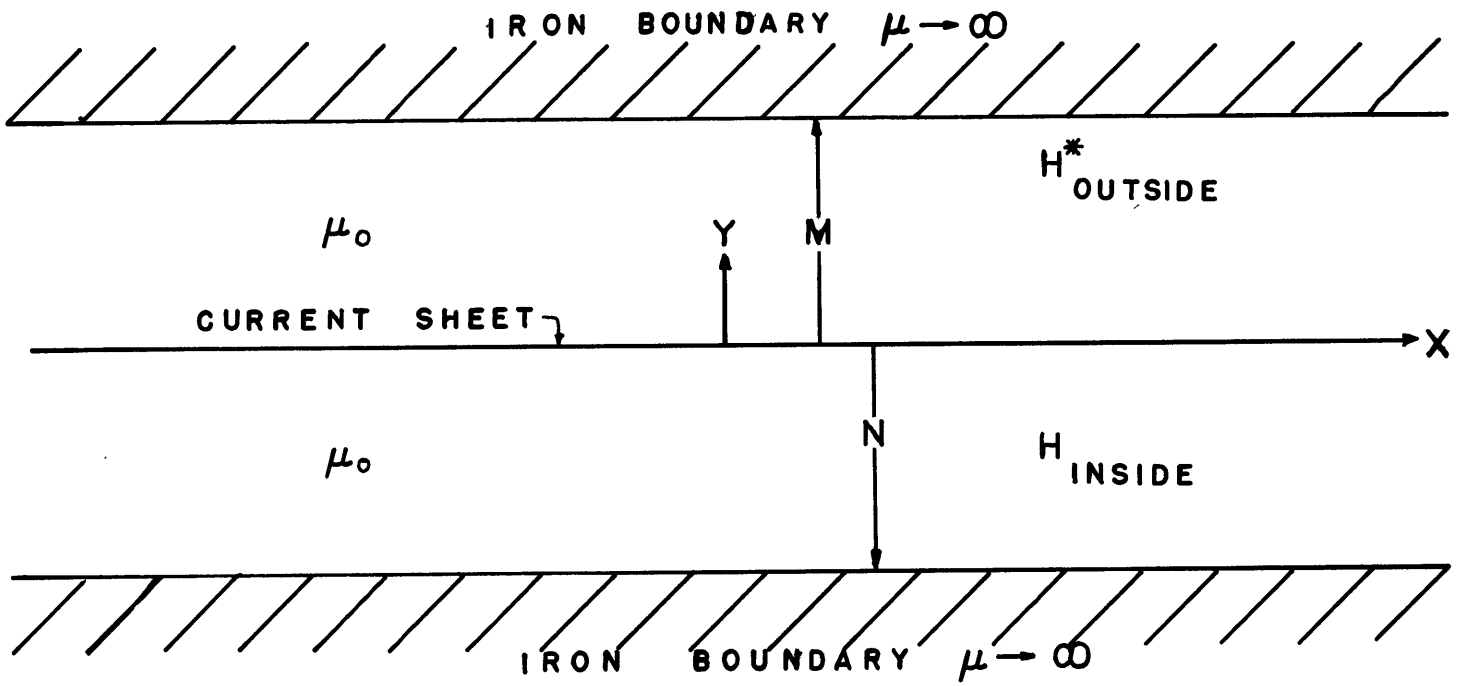

FIG. 17 CONFIGURATION FOR SOLUTION OF MAGNETIC FIELDS

current sheet joining the two regions. They are:

1) $\bar{n} \cdot (\bar{H} - \bar{H}^*) = 0$ across the current sheet

at $y = 0$ $\quad H_{y_{inside}} = H_{y_{outside}}^*$

2) $\bar{n} \times (\bar{H}^* - \bar{H}) = \bar{K}$ across the current sheet

at $y = 0$ $\quad H_{x_{inside}}^* - H_{x_{outside}} = -K_n \cos \frac{n\pi x}{l}$

3) $H_x^* = 0$ at upper iron boundary

$y = M$

4) $H_x = 0$ at lower iron boundary

$y = N$

The equation $\bar{H} = -\nabla\Phi = \frac{-\partial\Phi}{\partial x}\,\bar{i}_x - \frac{\partial\Phi}{\partial y}\,\bar{i}_y$ along with the boundary conditions gives us enough equations to solve for the unknown constants, and thus for the fields. In the region $0 < y < M$,

$$H^* = \frac{K_n}{2} \frac{(1+e^{-2\lambda N})}{(e^{-2\lambda M}-e^{-2\lambda N})} \left[(e^{-\lambda y}-e^{\lambda(y-2M)})\cos(\lambda x)\,\bar{i}_x - (e^{\lambda(y-2M)}+e^{-\lambda y})\sin(\lambda x)\right]\bar{i}_y$$

and in the region $0 < y < N$,

$$H = \frac{K_n}{2} \frac{(1+e^{-2\lambda M})}{(e^{-2\lambda M}-e^{-2\lambda N})} \left[(e^{-\lambda y}-e^{\lambda(y-2N)})\cos(\lambda x)\,\bar{i}_x - (e^{\lambda(y-2N)}+e^{-\lambda y})\sin(\lambda x)\right]\bar{i}_y$$

Full expressions for the fields are found by summing the Fourier components of K_n and then integrating over all of the differential current sheets to form a winding of finite thickness (Figure 18). To find the fields within

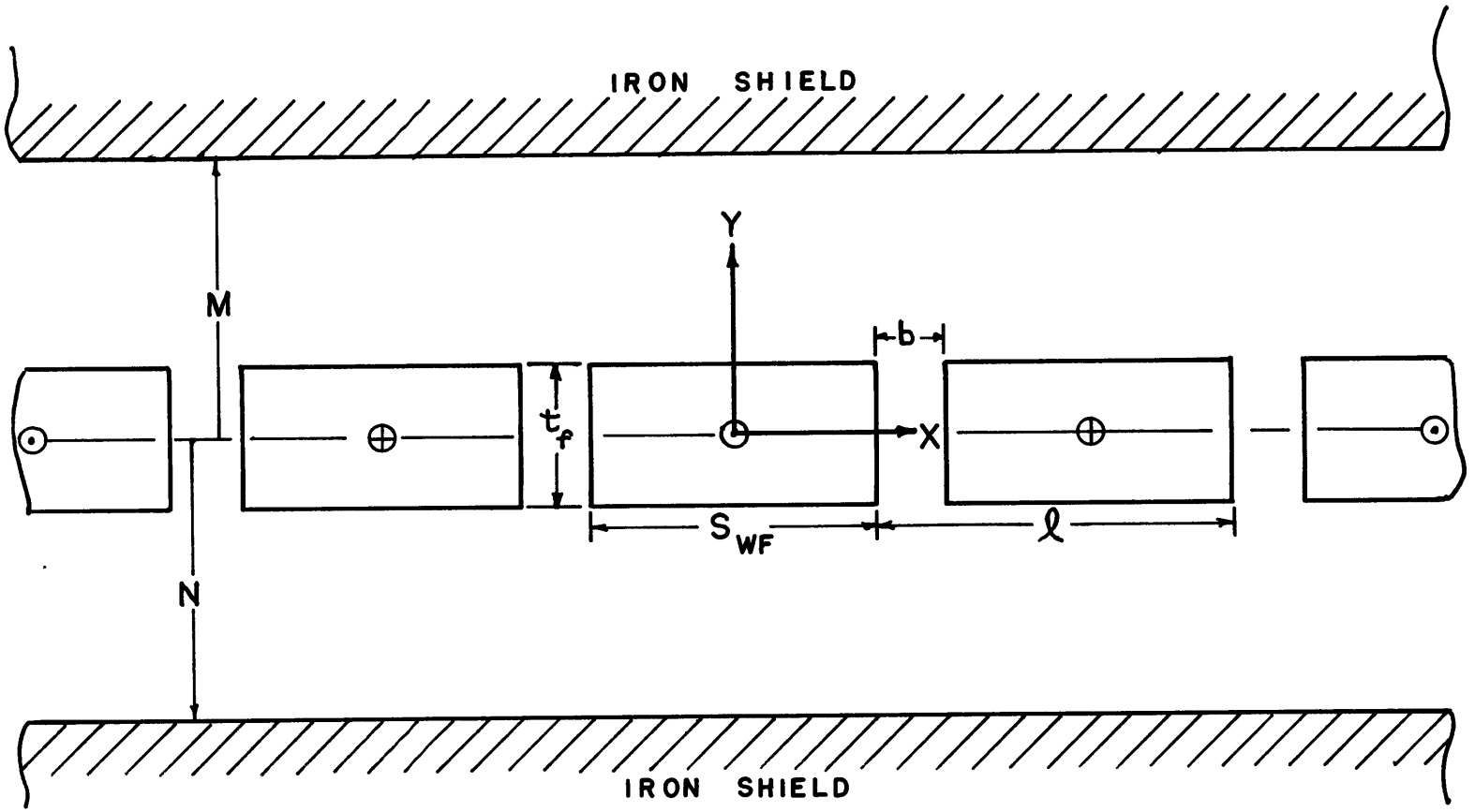

FIG. 18 CONFIGURATION OF FULL FIELD WINDING

the winding the fields due to current sheets in opposite regions must be superimposed, because the solutions are of Laplace's equation in a current-free region. The solutions for the fields in a current-carrying region may be solved directly by solution of Poisson's equation. This is not done here. An excellent treatment of these problems can be found in a book by B. Hague[6].

Region I)

$$H_i = \int_{-t/2}^{+t/2} H_i \, dy \qquad N \leq y \leq -t/2$$

Region II)

$$H = \int_{-t/2}^{y} H_o^* \, dy + \int_{y}^{+t/2} H_i \, dy \qquad -t/2 \leq y \leq +t/2$$

Region III)

$$H_o = \int_{-t/2}^{+t/2} H_o^* \, dy \qquad +t/2 \leq y \leq M$$

The results of these integrations are tabulated in Table of Chapter II.

II. Inductance Expressions

Inductances are determined from the flux linked by the armature and field windings. First the flux linked by a differential full pitch coil element is calculated. The differential number of turns in a differential element is given by:

$$d^2N = \frac{N_t}{A} \, dA$$

For this geometry see Figure I .

$$d^2N = \frac{N_t}{S_{wa} t_a} \, du \, dy$$

This is for the mutual flux linkage between armature phase "A" and the field winding. Field flux linked by this element and its full pitch complimentary element can be found by integrating the component of the field in the y direction over the straight line contour between the two elements.

$$d^2\lambda = L\, d^2N \int_u^{u+\ell} \mu_o H_{yfo}(x,y)du$$

Flux linked by the whole armature phase "A" winding can then by found by integrating the flux linked by the differential elements over the area of the whole winding.

$$\frac{\lambda_m}{L} = \int_{g+\frac{t_f}{2}}^{g+\frac{t_f}{2}+t_a} \int_{-\frac{S_{wa}}{2}}^{+\frac{S_{wa}}{2}} \frac{N_{ta}}{S_{wa}t_a}\left[\int_u^{u+\ell} \mu_o H_{yfo}(u,y)\, du\right] du\, dy$$

The self-inductance of the field winding and the mutual inductance of armature phase "A" with armature phase "B" are derived in a similar fashion.

$$\frac{\lambda_f}{L} = \int_{-t_f/2}^{+t_f/2} \int_{-\frac{S_{wf}}{2}}^{+\frac{S_{wf}}{2}} \frac{N_{ft}}{S_{wf}t_f}\left[\int_x^{x+\ell} \mu_o H_{yf_w}(\xi,y)d\xi\right] dx\, dy$$

$$\frac{\lambda_{ab}}{L} = \int_{\frac{t_f}{2}+g}^{\frac{t_f}{2}+g+t_a} \int_{\frac{2\ell}{3}-\frac{S_{wa}}{2}}^{\frac{2\ell}{3}+\frac{S_{wa}}{2}} \frac{N_{ta}}{S_{wa}t_a}\left[\int_u^{u+\ell} \mu_o H_{yaw}(u,y)du\right] du\, dy$$

The results of these integrations are listed in Table III. All of these expressions are inductances per pole pair and per unit length.

APPENDIX B

Limiting Analysis of Cylindrical Expressions

The validity of the field and inductance expressions for a linear winding geometry can be checked from the cylindrical expressions. As the radius and the number of pole pairs of a cylindrical machine increase, it should begin to look more and more like a linear machine. We can show these two expressions are identical in the limit as the radius and pole pairs approach infinity. This is true for all the field intensity and inductance expressions. This limiting process is done for one of the simpler field intensity expressions as an example. The other expressions are done in a similar manner, but they become quite involved and tedious. All of the cylindrical expressions reduced to the corresponding linear expressions in the limit.

We will use the expression for the radial field intensity outside of the field winding volume, H_{rfo}, as an example. In cylindrical coordinates, $R_{fo} < r < R_s$

$$H_{rfo} = \sum_{n\ \text{odd}} \frac{2J_f \sin(\frac{np\theta_{wf}}{2}) \sin np(\theta - \phi)}{n\pi(2 + np)} r\left(\frac{R_{fo}}{r}\right)^{np+2} \times$$

$$(1 - y^{np+2})\left[1 + \left(\frac{r}{R_s}\right)^{2np}\right]$$

let $R_s = R_m + M$ $\quad R_{fi} = R_m - t_f/2$

$R_{fo} = R_m + t_f/2$ $\quad r = R_m + y$ $\quad$ and $R_m = \frac{p\ell}{\pi}$

$$H_{rfo} = -\sum_{n\,odd} \frac{2J_f \sin\left(\frac{mp\theta_{wf}}{2}\right) \sin mp(\theta-\phi)}{n\pi(2+mp)} \left[\frac{\left(R_m+\frac{t_f}{2}\right)^{mp+2} - \left(R_m-\frac{t_f}{2}\right)^{mp+2}}{(R_m+Y)^{mp+2}}\right]$$

$$\times \left\{1 + \left[\frac{(R_m+Y)^{2mp}}{(R_m+M)^{2mp}}\right]\right\}$$

$$R_m = \frac{p\ell}{\pi}$$

$$= -\sum_{n\,odd} \frac{2J_f \sin\left(\frac{mp\theta_{wf}}{2}\right) \sin mp(\theta-\phi)}{n\pi(2+mp)} \left\{\frac{\left(\frac{p\ell}{\pi}\right)^{mp+2}\left[1+\left(\frac{\pi t_f}{2\ell}\right)\right]^{mp+2} - \left(\frac{p\ell}{\pi}\right)^{mp+2}\left[1-\left(\frac{\pi t_f}{2\ell}\right)\right]^{mp+2}}{\left(\frac{p\ell}{\pi}\right)^{mp+1}\left(1+\frac{\pi Y}{p\ell}\right)^{mp+1}}\right\}$$

$$\times \left\{1 + \frac{\left(\frac{p\ell}{\pi}\right)^{2mp}\left(1+\frac{\pi Y}{\ell p}\right)^{2mp}}{\left(\frac{p\ell}{\pi}\right)^{2mp}\left(1+\frac{\pi M}{\ell p}\right)^{2mp}}\right\}$$

$$= -\sum_{n\,odd} \frac{2J_f \sin\left(\frac{mp\theta_{wf}}{2}\right) \sin mp(\theta-\phi)\, p\ell}{n\pi^2(2+mp)} \left\{\frac{\left[1+(mp+2)\frac{\pi t_f}{2\ell p}+\cdots\right] - \left[1-(mp+2)\frac{\pi t_f}{2\ell p}+\cdots\right]}{\left[1+(mp+1)\left(\frac{\pi Y}{p\ell}\right)+(mp+1)(mp)\left(\frac{\pi Y}{\ell p}\right)^2\frac{1}{2!}+\cdots\right]}\right\}$$

$$\times \left\{1 + \frac{\left[1+(2mp)\left(\frac{\pi Y}{\ell p}\right)+\frac{(2mp)(2mp-1)}{2!}\left(\frac{\pi Y}{\ell p}\right)^2+\cdots\right]}{\left[1+(2mp)\left(\frac{\pi M}{\ell p}\right)+\frac{(2mp)(2mp-1)}{2!}\left(\frac{\pi M}{\ell p}\right)^2+\cdots\right]}\right\}$$

$$= -\sum_{n\,odd} \frac{2J_f \sin\left(\frac{mp\theta_{wf}}{2}\right) \sin mp(\theta-\phi)\, \ell p}{n\pi^2} \left\{\frac{\left[(2)\left(\frac{\pi t_f}{2\ell p}\right)+(2)(m+\frac{1}{p})(m)(\frac{1}{p})\left(\frac{\pi t_f}{2\ell}\right)^3\frac{1}{3!}+\cdots\right]}{\left[1+(m+\frac{1}{p})\left(\frac{\pi Y}{\ell}\right)+(m+\frac{1}{p})(m)\left(\frac{\pi Y}{\ell}\right)^2\frac{1}{2!}+\cdots\right]}\right\}$$

$$\times \left\{1 + \frac{\left[1+\left(2m\frac{\pi Y}{\ell}\right)+2m\frac{(2m-\frac{1}{p})}{2!}\left(\frac{\pi Y}{\ell}\right)^2+\cdots\right]}{\left[1+\left(2m\frac{\pi M}{\ell}\right)+\frac{(2m)(2m-\frac{1}{p})}{2!}\left(\frac{\pi M}{\ell}\right)^2+\cdots\right]}\right\}$$

$$\lim_{\substack{R_m \to \infty \\ P \to \infty}} H_{rfo} = -\sum_{n\,odd} \frac{4 J_f \ell}{n\pi^2} \sin\frac{n\pi S_{wf}}{2\ell} \sin\frac{n\pi x}{\ell} \left\{ \frac{\left[\left(\frac{\pi t_f}{2\ell}\right) + \frac{n^2}{3!}\left(\frac{\pi t_f}{2\ell}\right)^3 + \frac{n^4}{5!}\left(\frac{\pi t_f}{2\ell}\right)^5 + \ldots\right]}{\left[1 + \left(\frac{n\pi y}{\ell}\right) + \left(\frac{n\pi y}{\ell}\right)^2 \frac{1}{2!} + \ldots\right]} \right\}$$

$$\times \left\{ 1 + \frac{\left[1 + \left(\frac{2n\pi y}{\ell}\right) + \left(\frac{2n\pi y}{\ell}\right)^2 \frac{1}{2!} + \ldots\right]}{\left[1 + \left(\frac{2n\pi M}{\ell}\right) + \left(\frac{2n\pi n}{\ell}\right)^2 \frac{1}{2!} + \ldots\right]} \right\}$$

$$= -\sum_{n\,odd} \frac{4 J_f \ell}{n\pi^2} \sin\left(\frac{n\pi S_{wf}}{2\ell}\right) \sinh\left(\frac{n\pi t_f}{2\ell}\right) \left[e^{\frac{n\pi}{\ell}(y-2M)} + e^{-\frac{n\pi y}{\ell}} \right] \sin\left(\frac{n\pi x}{\ell}\right)$$

$$\lim_{\substack{R_m \to \infty \\ P \to \infty}} H_{rfo} = H_{yfo}$$

APPENDIX C

Alternative Designs

Optimum Winding Angle

Other attempts were made at designing large, multipole, superconducting machines by optimizing the design and placement of the active electrical components. An analysis was done to determine the optimum field winding angle for a given amount of superconductor. Optimum, in this case, was the geometric configuration that created the maximum total flux passing into the air gap. The field winding cross-sectional area for one pole is:

$$\frac{\theta_{wf}}{2}\left(R_{fo}^{\ 2} - R_{fi}^{\ 2}\right) = A$$

We wish to maximize

$$\Phi = \int_{\theta=0}^{\theta=\pi/2} B_r(\theta, r = R_{fo}) r d\theta$$

We must fix one other independent parameter. For a given tip speed and mechanical frequency we can fix the outside field radius, R_{fo}.

The expression for total flux passing into the air gap can be non-dimensionalized by defining a non-dimensional parameter, β.

$$\beta = \frac{2A}{R_{fo}^{\ 2}}$$ where A = cross-sectional field winding area of one pole.

To optimize Φ with respect to θ_{wf},

$$\frac{\partial \Phi}{\partial \theta_{wf}} = 0, \quad \text{solve for } \theta_{wf}.$$

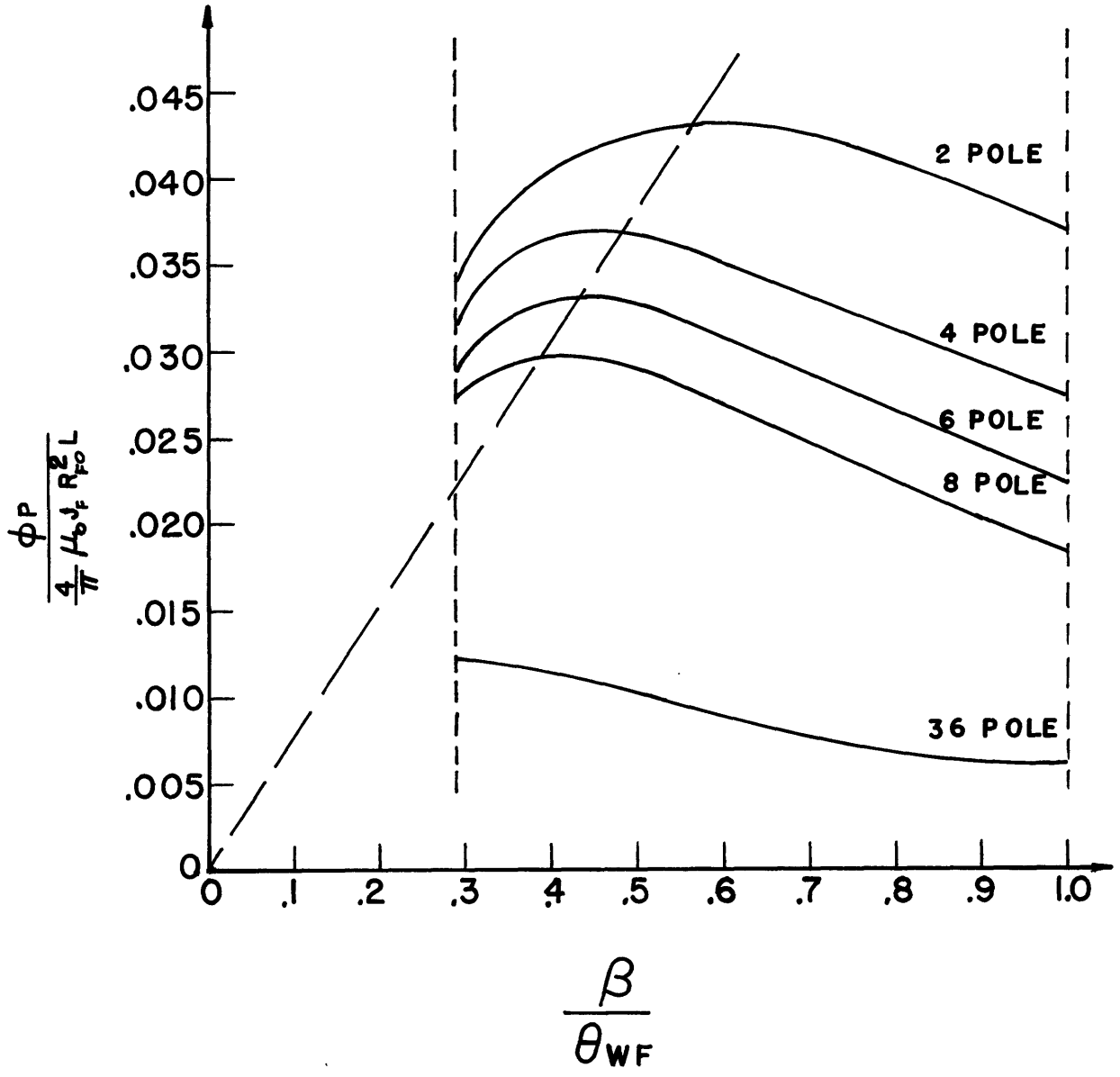

FIG. 19 OPTIMUM WINDING ANGLE

This can be determined implicitly,

$$\frac{np}{(2+np)}\,\frac{1}{\beta}\left[\frac{1-(1-\beta/\theta_{wf})^{\frac{np+2}{2}}}{(1-\beta/\theta_{wf})^{np/2}}\right]=\frac{\tan\left(\frac{np\theta_{wf}}{2}\right)}{\theta_{wf}^{2}}$$

Figure 19 shows non-dimensional flux plotted versus winding angle with β held constant. It demonstrates that there is a winding angle that yields maximum radial flux in the air gap. The curve is cut off on the left end due to the fixed area constraint and on the right end because the inside field radius goes to zero. If we compare the net flux increase we gain by using the optimum winding angle for first harmonic fields, with the winding angle that yields zero third harmonic flux, i.e. 120 electrical degrees, the percentage range of increase is approximately zero to ten percent. The advantage of increasing the radial flux into the air gap by careful winding angle design is attenuated by the resultant third harmonic fields due to winding angles other than 120 electrical degrees. It appears that there is not much advantage in using winding angles other than those required to eliminate higher harmonic fields.

REFERENCES

1. J.L. Kirtley, Jr., "Design and Construction of an Armature for an Alternator With a Superconducting Field Winding," Ph.D. Thesis, Dept. of Electrical Engineering, M.I.T., August, 1971.

2. D. Greeneisen, "A Design Program for Superconducting Electrical Machines," M.S.E.E. and Nav.E. Thesis, Dept. of Naval Architecture and Marine Engineering, M.I.T., June, 1968.

3. D.L. Luck, "Electromechanical and Thermal Effects of Faults Upon Superconducting Generators," Ph.D. Thesis, Dept. of Electrical Engineering, M.I.T., June, 1971.

4. H.H. Woodson and J.R. Melcher, Electromechanical Dynamics, Parts I and II, Wiley, New York, 1968.

5. A.E. Fitzgerald, C. Kingsley, Jr., and A. Kusko, Electric Machinery, Third edition, McGraw-Hill, New York, 1971.

6. B. Hague, The Principles of Electromagnetism Applied to Electrical Machines, Dover, New York, 1962.

7. H.L. Seward, Ed., Marine Engineering, Vol. I, SNAME, New York, 1942.

8. V.L. Streeter, Ed., Handbook of Fluid Dynamics, McGraw-Hill, New York, 1961.

9. T. Baumeister, Ed., Standard Handbook for Mechanical Engineers, 7th edition, McGraw-Hill, New York, 1967, pp. 11-53 to 11-54.

10. T. Hannan, Strategy of Propeller Design, Thomas Reed Publications, London, Sunderland, Glasgow.

TABLE V REFERENCES

1. H.H. Woodson, Z.J.J. Stekly, and E. Halas, "A Study of Alternators with Superconducting Field Windings: I - Analysis, II - Experiment," IEEE Trans. on Power Apparatus and Systems, Vol PAS-85, No. 3, March, 1966, pp. 264-280.

2. P. Thullen, J.C. Dudley, D.L. Greene, J.L. Smith, Jr., and H.H. Woodson, "An Experimental Alternator With a Superconducting Rotating Field Winding," IEEE Trans. Power Apparatus and Systems, Vol. PAS-90, No. 2, March/April, 1971, pp. 611-613.

3. A.S. Veselovskiy, et. al., "100 KW A.C. Generator With Superconducting Inductor," I.V. Kurchatov, Inst. of Atomic Energy, Rep. 2182, Moscow, 1972.

4. Private Communication

5. J.L. Kirtley, Jr., J.L. Smith, Jr., P. Thullen, and H.H. Woodson, "MIT - EEI Program on Large Superconducting Machines," IEEE Trans. Power Apparatus and Systems, Vol. PAS-92, No. 4, July/August, 1973.

6. T.J. Fagan, Jr., et. al., "Development of a 5 MVA Superconducting Generator, Mechanical and Cryogenic Design," IEEE Winter Power Meeting, C 73 255-7, New York, 1973.

7. C.J. Mole, et. al., "Electric Propulsion Machinery Study," Final Report, Contract No. N00014-72-c-0393, Office of Naval Research, NR 097-386/12-14-72, March, 1973.

8. J.V. Minervini, "Analysis and Design of Multipole, Superconducting Rotating Electric Machines for Ship Propulsion," S.M.M.E. Thesis, Dept. of Mechanical Engineering, M.I.T., February, 1974.

9. A.D. Appleton and A.F. Anderson, "A Review of the Critical Aspects of Superconducting A.C. Generators," Proceedings of the 1972 Applied Superconductivity Conference, May 1-3, Annapolis, Maryland, pp. 136-144.

10. D.L. Luck, "Electromechanical and Thermal Effects of Faults Upon Superconducting Generators," Ph.D. Thesis, Dept. of Electrical Engineering, M.I.T., June, 1971.

11. M.J. Jefferies, E.E. Gibbs, G.R. Fox, C.H. Holley, D.M. Willyoung, "Prospects for Superconductive Generators

TABLE V REFERENCES

(Continued)

in the Electric Utility Industry," IEEE Trans. Power Apparatus and Systems, Vol. PAS-92, No. 5, pp. 1659-69.

12. H.H. Woodson, et. al., "The Application of Superconductors in the Field Windings of Large Synchronous Machines", IEEE Trans. Power Apparatus and Systems, Vol. PAS-90, No. 2, March/April pp. 620-627.

13. Private Communication

14. J.K. Hulm, et. al., "Development of a 5 MVA Superconducting Generator, General Aspects," Presented at the 1973 IEEE Winter Power Meeting, New York, January, 1973, C73 245-8.